bioRxiv preprint doi: https://doi.org/10.1101/649913; this version posted October 22, 2019. The copyright holder for this preprint (which was not certified by peer review) is the author/funder. All rights reserved. No reuse allowed without permission.

Mechanisms of chromosome biorientation and bipolar spindle assembly analyzed by computational modeling

Christopher J. Edelmaier, Adam R. Lamson, Zachary R. Gergely,
Saad Ansari, Robert Blackwell, J. Richard McIntosh, Matthew A. Glaser,
and Meredith D. Betterton*

Department of Physics
University of Colorado, Boulder, CO 80309, USA
*To whom correspondence should be addressed; E-mail: mdb@colorado.edu.

Abstract

The essential functions required for mitotic spindle assembly and chromosome biorientation and segregation are not fully understood, despite extensive study. To illuminate the combinations of ingredients most important to align and segregate chromosomes and simultaneously assemble a bipolar spindle, we developed a computational model of fission-yeast mitosis. Robust chromosome biorientation requires progressive restriction of attachment geometry, destabilization of misaligned attachments, and attachment force dependence. Large spindle length fluctuations can occur when the kinetochore-microtubule attachment lifetime is long. The primary spindle force generators are kinesin-5 motors and crosslinkers in early mitosis, while interkinetochore stretch becomes important after biorientation. The same mechanisms that contribute to persistent biorientation lead to segregation of chromosomes to the poles after anaphase onset. This model therefore provides a framework to interrogate key requirements for robust chromosome biorientation, spindle length regulation, and force generation in the spindle.

Introduction

Cell biology seeks to understand how nanometer-scale molecules organize micron-scale cells, a question well-suited to theory and modeling [1]. As quantitative cell biology has grown, modeling has expanded in scope [2]. Theory and simulation can now predict cellular phenomena across length and time scales, giving new insight into cellular self-organization. In the cytoskeleton, an important challenge is understanding how a relatively small number of building blocks can produce diverse structures and machines. Quantitative modeling has contributed to our understanding of cytoskeletal functions including mitosis [3,4], cytokinesis [5,6], and cell motility [7,8].

Chromosome segregation in eukaryotes is performed by the mitotic spindle, a self-organized microtubule (MT)-based machine [9,10]. Dynamic spindle MTs are typically organized with their plus-ends toward the center of the spindle, forming a bipolar array as the spindle poles move apart (Figure 1) [10,11].

bioRxiv preprint doi: https://doi.org/10.1101/649913; this version posted October 22, 2019. The copyright holder for this preprint (which was not certified by peer review) is the author/funder. All rights reserved. No reuse allowed without permission.

Motor proteins and crosslinkers that bundle and slide MTs create, extend, and stabilize MT bundles (Figure 1A,B) [12–20]. As the spindle assembles, MTs attach to duplicated chromosomes at kinetochores and align them at the spindle midzone (Figure 1A-C) [21–23]. Biorientation occurs when sister kinetochores are attached to sister poles, but is often preceded by erroneous attachment (Figure 1D) [24–28]. Kinetochores therefore perform multiple functions: they link chromosomes to MTs, maintain attachment to MT ends under force and as MTs grow and shrink, sense MT attachment and tension between sisters, and regulate correction of attachment errors and the spindle-assembly checkpoint [21, 29].

It is not fully understood how kinetochores, microtubules, and associated proteins robustly assemble a bipolar spindle and align chromosomes. In particular, it is unclear which kinetochore functions are most important for error correction and proper chromosome segregation [28, 29]. Error correction is affected by kinetochore geometry [26,30–33] and attachment/tension sensing [21,29,34,35], although the relative contribution of different effects is not established [36–39]. Destabilization of incorrect attachments by Aurora B kinase appears to be particularly important for high-fidelity chromosome segregation [40–43]. Therefore, further insight into the minimal mechanisms required for spindle assembly and chromosome biorientation could be gained from a computational model.

Once the spindle assembles and attaches to chromosomes, it achieves a consistent length [44–48]. The force-balance model proposes that outward-directed forces from plus-end directed sliding motors separate spindle poles, while inward-directed forces from minus-end directed sliding motors and chromosomes pull the poles together [49]. This model helps explain perturbations that alter spindle length [15, 46, 50, 51]. However, a change in spindle length may occur from a direct change in force production or from indirect effects such as alteration in MT dynamics or alignment [15, 52]. In addition, the steady-state force-balance model requires extension to address spindle length fluctuations, in which the bipolar spindle assembles, but then undergoes large, dynamic length changes [50,52–58]. Computational modeling can be a valuable tool to dissect force generation and spindle length changes.

To better understand the key mechanistic requirements for chromosome biorientation and how kinetochore number and attachment affect spindle length stability, we developed a computational model of fission-yeast mitosis. *Schizosaccharomyces pombe* cells are amenable to genetic manipulation and quantitative experiments [59–63] and the spindles are small enough that full 3D simulations are computationally tractable [59, 63–65]. We were motivated by previous work modeling spindle function and chromosome segregation [3,4]. Because we study de novo spindle assembly and chromosome alignment, we could not use previous models that started with an already-bipolar structure and/or chromosomes attached to the spindle. Therefore we extended a previous model of spindle assembly in the absence of chromosomes and kinetochore-microtubule attachments [63, 65, 66] to include chromosomes and kinetochores.

Our model successfully accomplishes spindle assembly and chromosome biorientation. The results give insight into key requirements for error correction and long-lived biorientation, emphasizing the importance of progressive restriction of attachment, destabilization of misaligned attachments, and force-dependent attachment lifetime. The turnover of kinetochore-MT attachments affects spindle mechanics, because models with larger attachment lifetime exhibit larger fluctuations in spindle length. The spindle components which contribute most to force generation change over time: initial spindle pole separation is due to the outward force from kinesin-5 motors overcoming the passive crosslinker braking force, while interkinetochore stretch is the main inward force after biorientation. Finally, properly constructed metaphase spindles are able to robustly segregate chromosomes in the model.

bioRxiv preprint doi: https://doi.org/10.1101/649913; this version posted October 22, 2019. The copyright holder for this preprint (which was not certified by peer review) is the author/funder. All rights reserved. No reuse allowed without permission.

Methods

Computational modeling has been used previously to study the mitotic spindle [3, 4, 67]. Recent work on spindle and MT organization includes studies of spindle elongation and force balance [59, 68], the formation and maintenance of antiparallel MT overlaps [69, 70], MT bundling and sliding [15], spindle movements and positioning [71, 72], spindle length and shape [15, 51, 52, 73, 74], MT organization [75], and spindle assembly from a bipolar initial condition [32, 76]. Models of kinetochore-MT attachment and biorientation have examined capture of lost kinetochores [63, 77], chromosome reorientation after MT attachment [31], attachment error correction [33, 39, 78, 79], and chromosome movement on the spindle [52, 61, 80–82]. Most spindle models have started with a bipolar structure or separated spindle poles, and most previous chromosome models have begun with chromosomes attached to the spindle or near a pre-formed spindle. Because we seek to model simultaneous spindle assembly and chromosome alignment with few imposed constraints, we developed a new model, building on previous work on spindle assembly in the absence of chromosomes and kinetochore-microtubule attachments [63, 65, 66].

In developing the model, we used 3-dimensional geometry and an initial condition with side-by-side centrosomes (spindle-pole bodies, or SPBs that mimics the biological configuration at the onset of mitosis. Because stochastic binding kinetics and turnover of motor proteins, crosslinkers, and kinetochore-MT attachments are important in spindle assembly and chromosome alignment, we developed methods to rapidly compute the statistical mechanics of protein binding and unbinding [63, 83–85]. The binding and unbinding of motors, crosslinkers, and kinetochore-MT attachments is microscopically reversible and force-dependent. Motor proteins move with force-dependent velocity, which can be important for force generation by crosslinking motors [63, 85]. We represent steric interactions between molecules (such as microtubules) with a hard-core short-range repulsive interaction, rather than soft repulsion. The simulations are based on Brownian dynamics, and state changes (such as motor binding/unbinding and an MT switching from growing to shrinking) are modeled using kinetic Monte Carlo [62, 63, 65, 66] (Appendix A, Tables 1, 3). We seek quantitative agreement between results from the simulation model and experiments, and so fix poorly constrained model parameters by direct comparison to data [63, 66].

Geometry, microtubules, motors, and crosslinkers

The simulation takes place within a sphere that represents the fission-yeast nucleus. Two SPBs are embedded in the nuclear envelope but free to move on the surface of the sphere (although we also consider effects of allowing SPBs to move radially due to a soft nuclear envelope, as discussed below). Each SPB nucleates 14 MTs, with their minus-ends tethered to the SPBs by a spring and which undergo dynamic instability at their plus-ends. Steric interactions mediated by short-range hard repulsion between MTs, SPBs, and the nuclear envelope (Figure 1A,B, Appendix A).

Three classes of motors and crosslinkers assemble the spindle (Figure 1A,B). Kinesin-5 motors (representing Cut7) move bidirectionally on MTs [86–89], with plus-end directed movement on antiparallel MTs exerting force to slide apart the SPBs. Kinesin-14 motors (representing Pkl1 and Klp2) crosslink MTs and one head walks toward the MT minus-ends, aligning MTs and exerting force that shortens the spindle [13–15, 90–93]. Crosslinkers (representing Ase1) preferentially bind antiparallel MTs [17, 18, 94–97] and stabilize MT overlaps when crosslinking near the end of an MT, an effect which mimics the recruitment of stabilizing proteins such as CLASP [53] to MT ends.

bioRxiv preprint doi: https://doi.org/10.1101/649913; this version posted October 22, 2019. The copyright holder for this preprint (which was not certified by peer review) is the author/funder. All rights reserved. No reuse allowed without permission.

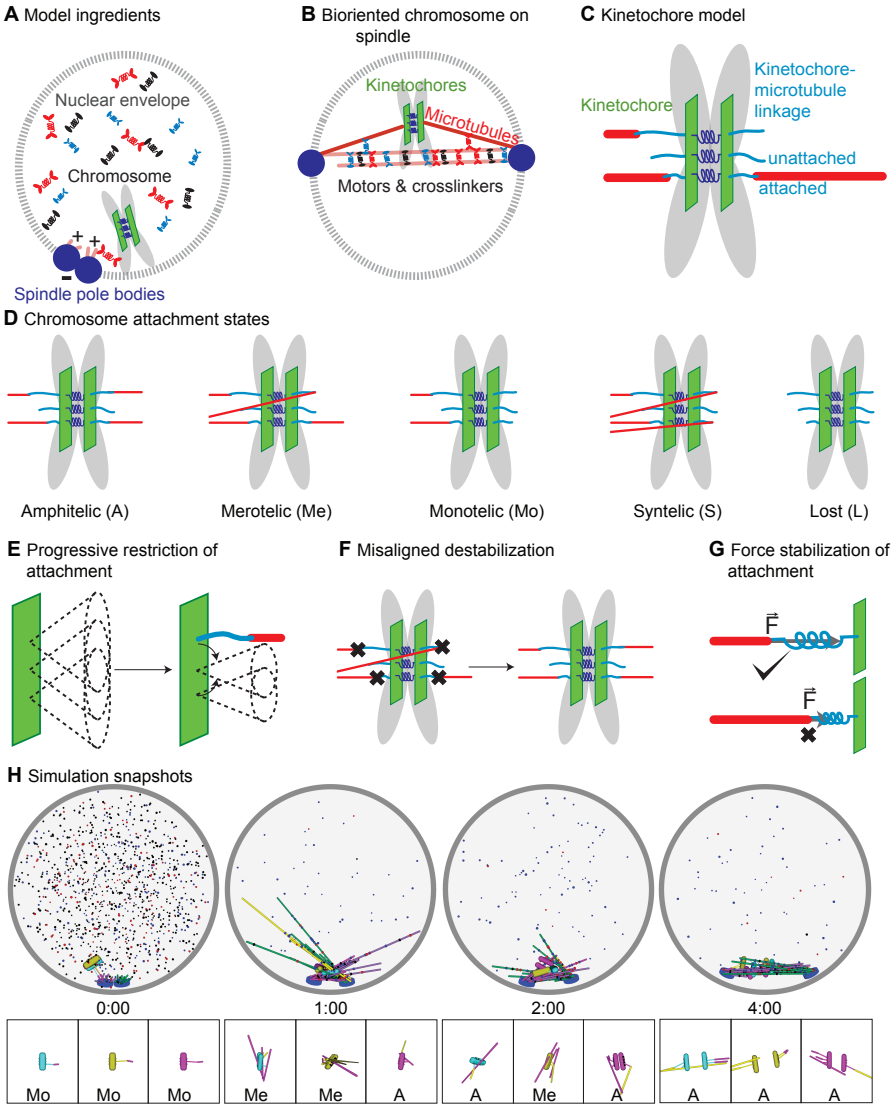

Figure 1: **Schematic of computational model and simulation of the reference model**. **(A)** Schematic of initial condition, showing adjacent spindle-pole bodies (blue) embedded in the nuclear envelope (gray dashed), proximal chromosomes (gray with green plate and blue springs), short microtubules (pink), and motor proteins and crosslinkers (red, blue, and black). **(B)** Schematic of bipolar spindle and a bioriented chromosome. **(C)** Schematic of chromosome and kinetochore model showing sister chromatids (gray), one kinetochore on each chromatid (green plates), the pericentric chromatin spring (blue springs), and kinetochore-MT attachment factor (blue line). **(D)** Schematic of chromosome attachment states, showing amphitelic, merotelic, monotelic, syntelic, and lost chromosomes. **(E)** Schematic of progressive restriction, showing that the angular range of kinetochore-MT attachment is restricted after attachment. **(F)** Schematic of misaligned destabilization of attachment, showing that misaligned attachments are destabilized. **(G)** Schematic of force stabilization of attachment, showing that end-on attachment to depolymerizing MTs has increased lifetime. **(H)** Image sequence of spindle assembly and chromosome biorientation rendered from a three-dimensional simulation. Initially, SPBs are adjacent (blue disks), MTs are short spherocylinders (green and purple when unattached to kinetochores, yellow and magenta when attached), and chromosomes (cyan, yellow, magenta) are near SPBs. Motors and crosslinkers are dispersed spots (red, blue, and black) within the nucleus (gray boundary). Time shown in minutes:seconds. Lower: a zoomed view of each chromosome with attachment state labeled.

bioRxiv preprint doi: https://doi.org/10.1101/649913; this version posted October 22, 2019. The copyright holder for this preprint (which was not certified by peer review) is the author/funder. All rights reserved. No reuse allowed without permission.

Chromosomes and kinetochores

We represent the multiple outer kinetochore proteins involved in MT binding [21, 29] by a single attachment factor that can be bound or unbound to an MT. Because fission-yeast kinetochores can bind up to 3 MTs [98], each kinetochore has 3 attachment factors in the model separated by 40 nm along the kinetochore plate (Figure 1C, Figure 9). Attachments are constrained so that no more than one attachment factor can bind to the same MT plus-end. The attachment factor is a 54-nm long spring that exerts force on the MT and kinetochore when stretched or compressed (Tables 4, 5). Attachment factors can make both lateral and end-on attachments to MTs, with different binding kinetics that favor end-on attachment. Importantly, the model includes tip tracking: a tip-bound attachment factor tracks MT ends by maintaining end-on attachment during MT growth and shrinking. The attachment factor also includes a plus-end-directed kinetochore motor, representing the measured contribution of kinetochore-localized dimeric Cut7 to chromosome alignment [99]. End-on attachment alters MT dynamic instability and is force-dependent, as measured previously [100, 101].

Physically each kinetochore is a rectangular plate of length 150 nm, width 50 nm, and zero thickness (Figure 1C) [98] with a steric repulsion with MTs. Sister kinetochores are linked via springs that resist stretching and rotation, to maintain the distance and alignment of the kinetochores (Figure 1C, Figure 9) [60, 102]. The pericentric DNA is represented as a spherocylinder of length 200 nm and diameter 75 nm, which has a soft repulsion with MTs that allows MT-chromatin overlap with an energy penalty (Appendix A).

With these ingredients, the model can achieve both correct and erroneous kinetochore-MT attachment states (Figure 1D). To achieve error correction and persistent biorientation, we found three key model ingredients were required: progressive restriction of attachment (Figure 1E), destabilization of misaligned attachment (Figure 1F), and stabilization of attachment by force (Figure 1G, Appendix A). With these mechanisms, the model exhibits both spindle assembly and chromosome biorientation (Figure 1H, Video S1).

Comparison to experimental results

To constrain model parameters, we developed multiple tests of simulation performance based on live-cell imaging, electron microscopy, and biorientation. First, we quantified the dynamics of spindle length and kinetochore position by confocal fluorescence light microscopy (Figure 2) [52, 63]. Cells with low-level labeling of MTs with *mCherry-atb2* [63, 103] and the *cen2-GFP* marker on the centromeric DNA of chromosome 2 [104] allowed imaging of spindle length and centromere position (Appendix A). The Cen2 marker is displaced only 125 nm on average from the kinetochore [105], allowing quantification of the position of a single pair of sister kinetochores. We measured spindle length and kinetochore position by fitting Gaussian spots and lines to detect features, and then tracked spindle length and kinetochore position over time using previous methods (Appendix A) [106]. Second, we used previously published electron tomographic reconstructions of fission yeast spindles [107, 108] to measure spindle structure [63]. Third, we quantified how successfully the models biorient chromosomes, measured by the fraction of simulation time during which all the chromosomes are bioriented and the average number of end-on attachments.

We combined these measures of simulation performance in a fitness function which quantifies the overall success of any set of model parameters. We then varied poorly constrained model parameters to

bioRxiv preprint doi: https://doi.org/10.1101/649913; this version posted October 22, 2019. The copyright holder for this preprint (which was not certified by peer review) is the author/funder. All rights reserved. No reuse allowed without permission.

maximize the fitness function. The optimized parameters defined the reference model (Appendix A).

Results

A computational model can assemble a bipolar spindle and biorient chromosomes

To understand the mechanisms most important for proper chromosome alignment on the spindle, we developed a computational model of fission-yeast mitosis (Figure 1) that includes spindle MTs nucleated from SPBs, crosslinking motors, passive crosslinkers, pericentric chromatin, and kinetochores, all contained within a spherical nucleus (Methods, Figure 1A,B). Kinetochore-MT binding occurs via attachment factors that represent MT-binding kinetochore proteins (Figure 1C), which can form both correct and erroneous MT-kinetochore attachments (Figure 1D). Kinetochore-MT attachments progressively restrict in angle as MTs bind (Figure 1E), a mechanism motivated by previous work on kinetochore geometry and chromosome rotation in error correction [26,30–33]. In particular, work on the *S. pombe* monopolin complex has proposed that monopolin acts as a site-clamp that co-orients MTs bound to the same kinetochore [30]. To correct attachment errors, we included destabilization of improper attachments and tip-enhanced catastrophe (Figure 1F), mimicking the activity of Aurora B kinase [41, 105, 109] and recapture of lost kinetochores by MT depolymerization [52, 107, 110–112]. To maintain biorientation, we implemented force-dependent kinetochore-MT attachment kinetics (Figure 1G), based on previous work that demonstrated an increase in attachment lifetime with tension when kinetochores are attached to depolymerizing MTs [100, 101]. For further details of the construction of the model, see Methods and Appendix A. With these ingredients, the model is able to spontaneously assemble a bipolar spindle starting with side-by-side SPBs, form MT-kinetochore attachments, correct attachment errors, and biorient the chromosomes (Figure 1H, Video S1).

To refine and test the model, we measured spindle assembly and chromosome alignment in fission yeast (Figure 2, Methods, Appendix A). We quantified spindle length, SPB-kinetochore separation, and interkinetochore stretch from the onset of mitosis until chromosome segregation (Figure 2A-D) and used these data to adjust model parameters (Methods, Appendix A). After refinement, simulations of the reference model showed dynamics of SPB separation, kinetochore movement along the spindle, and interkinetochore stretch similar to the experimental data (Figure 2E-H, Video S2). As occurs in cells, the dynamics varied from simulation to simulation, but were similar on average (Figure 2I, Figure 10).

Single model perturbations recapitulate the requirement for kinesin-5 motors and CLASP

After developing the reference model, we verified that single model perturbations recapitulate results from fission-yeast genetics. Kinesin-5 motors are essential for spindle assembly in *S. pombe*, and temperature-sensitive mutants of the kinesin-5/Cut7 fail to separate spindle-pole bodies [93, 113–115]. Consistent with this, when we remove kinesin-5 from the model, SPBs do not separate (Figure 2J). Similarly, the microtubule-associated protein CLASP is essential for spindle assembly in fission yeast, where it is recruited to MT antiparallel overlaps by Ase1 and stabilizes MT dynamics [53]. When the stabilization of dynamics of crosslinked MTs is turned off in the model, SPBs do not separate (Figure 2K). Chromosome biorientation is abolished in models where the SPBs do not separate (Figure 2L, Video S2).

We further studied combined perturbations (Figure 3) by varying kinesin-5 and crosslinker number in the absence of kinesin-14 (Figure 3A) and by varying kinesin-5 and -14 number in the absence of

bioRxiv preprint doi: https://doi.org/10.1101/649913; this version posted October 22, 2019. The copyright holder for this preprint (which was not certified by peer review) is the author/funder. All rights reserved. No reuse allowed without permission.

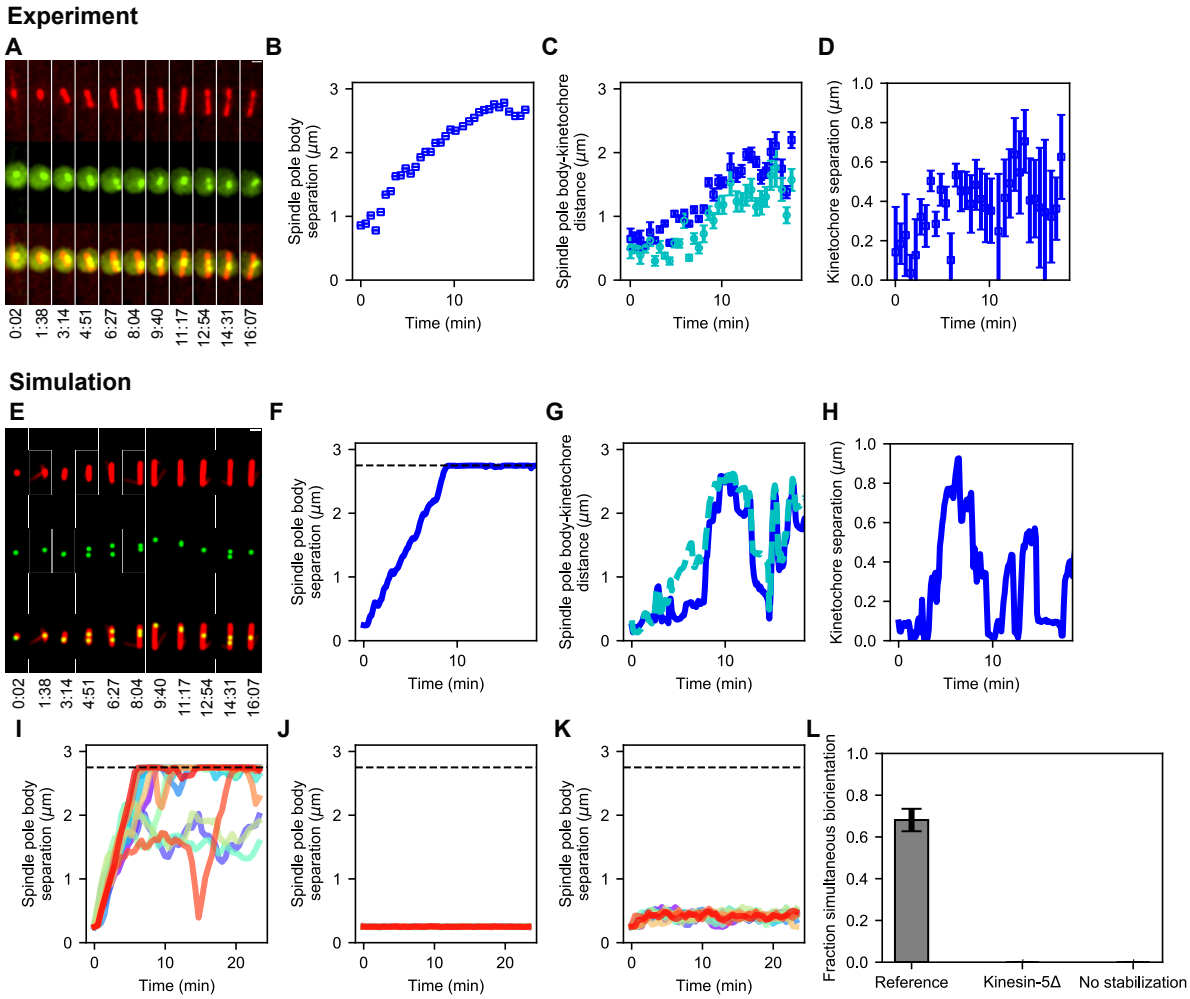

Figure 2: **Comparison of spindle assembly and chromosome alignment in cells and simulations.** **(A-D)** Experimental results. **(A)** Maximum-intensity projected smoothed images from time-lapse confocal fluorescence microscopy of fission yeast with *mCherry-atb2* labeling MTs (red) and *cen2-GFP* labeling the centromere of chromosome 2 (green). Time shown in minutes:seconds. **(B)** Spindle length, **(C)** spindle pole body-kinetochore distance, and **(D)** interkinetochore distance versus time from the experiment shown in (A). **(E-K)** Simulation results. **(E)** Simulated fluorescence microscopy images with MTs (red) and a single kinetochore pair (green). **(F)** Spindle length, **(G)** spindle pole body-kinetochore distance, and **(H)** interkinetochore distance versus time from the simulation shown in (E), sampled at a rate comparable to the experimental data in (A-D). Note that the rigid nucleus in our model sets an upper limit on spindle length of 2.75 μm, as shown by the dashed line in F. **(I)** Spindle length versus time for 12 simulations of the reference model. **(J)** Spindle length versus time for 12 simulations in a model lacking kinesin-5. **(K)** Spindle length versus time for 12 simulations in a model lacking crosslink-mediated microtubule stabilization. **(L)** Fraction simultaneous biorientation for the reference, kinesin-5 delete, and no-stabilization models (N = 12 simulations per data point).

crosslinkers (Figure 3B). Kinesin-14 in our models combines the functions of fission-yeast Pkl1 and Klp2, neglecting the anchoring of MT minus-ends to SPBs by Pkl1 previously measured [91–93, 116].

bioRxiv preprint doi: https://doi.org/10.1101/649913; this version posted October 22, 2019. The copyright holder for this preprint (which was not certified by peer review) is the author/funder. All rights reserved. No reuse allowed without permission.

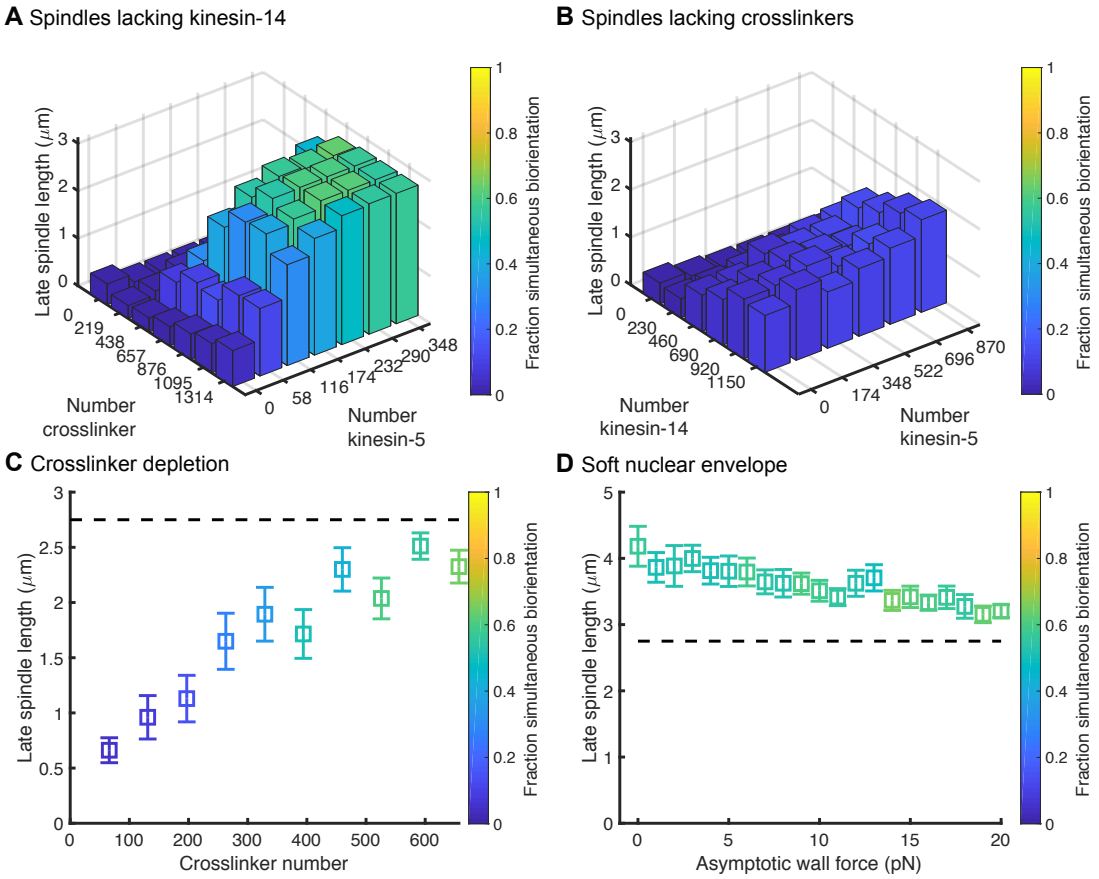

Figure 3: **Figure supplement to figure 2: Results of simulations with perturbations to motor and crosslinker number and nuclear envelope.** (**A**) Simulated spindles form and biorient chromosomes in the absence of kinesin-14 motors if kinesin-5 and crosslinker number are increased. (**B**) Simulated spindles have difficulty forming in the absence of crosslinkers, and do not properly biorient chromosomes. (**C**) Variation of spindle length with crosslinker number, showing that spindle length changes slowly with number of crosslinkers. (**D**) Spindle length as a function of wall force for a model of a soft nuclear envelope for which the SPBs are not fixed on the surface of the sphere. The reference model contains 174 kinesin-5 motors, 230 kinesin-14 motors, and 657 crosslinkers. (N = 12 simulations per data point.)

Experimentally, cells lacking Klp2 or both Pkl1 and Klp2 do not show altered average spindle length [50, 90]. Consistent with this, model spindles formed and bioriented chromosomes in the absence of kinesin-14, and spindle length depended on the ratio of kinesin-5 to crosslinkers.

In fission yeast, Ase1 deletion cells assemble spindles [17, 50, 117], but the Ase1-Klp9 double deletion is lethal [117]. Although Klp9 is a tetrameric motor, recent work found that it also has a non-motor crosslinking function that is important for spindle integrity [117]. This suggests that in the absence of Ase1, Klp9's MT crosslinking function In our model, the physical crosslinkers include the function of both Ase1 and Klp9 in the cell. Therefore, we would expect that deleting both Ase1 and Klp9 is equivalent to completely removing crosslinkers from our model, but that deleting Ase1 alone is approximately equivalent to removing half the crosslinkers from our model (because Ase1 dimers and Klp9 tetramers

bioRxiv preprint doi: https://doi.org/10.1101/649913; this version posted October 22, 2019. The copyright holder for this preprint (which was not certified by peer review) is the author/funder. All rights reserved. No reuse allowed without permission.

are present in approximately equal numbers in the cell [118]). To test this, we varied total crosslinker number in the model (Figure 3C). Completely removing crosslinkers abolishes spindle assembly because spindles cannot maintain robust antiparallel MT overlaps, consistent with the experimental lethality of the Ase1-Klp9 double deletion [117]. Similarly, removing half the crosslinkers leads to slightly shorter spindles mild biorientation problems, consistent with experimental results with Ase1 deletion [17, 50].

Most of our simulations represent the nuclear envelope as a rigid sphere with the SPBs constrained to move on the surface of this sphere. However, constraining SPBs to a fixed radius alters force balance on the spindle and may alter spindle length. Therefore, we tested a model of a soft nuclear envelope by allowing the SPBs to move radially in a potential that mimics the energy required to deform the nuclear envelope [65, 66] (Methods, Appendix A). The results show that a soft nuclear envelope leads to slightly longer spindles (Figure 3D, Video S3), but for a physically realistic nuclear envelope force of around 17 pN, spindle length remains near 3 μm, as measured experimentally.

Chromosome biorientation during spindle assembly requires three basic kinetochore properties

Our simulations start in a state mimicking early mitosis with monotelic chromosomes, then spontaneously assemble a bipolar spindle and biorient chromosomes. Biorientation requires the model to correct attachment errors and maintain correct attachments. This occurs in the simulations primarily through progressive restriction of attachment angle, misaligned destabilization, and force-dependent kinetochore-MT attachment.

Kinetochores can avoid merotelic attachments by progressive restriction of microtubule binding

To facilitate correct initial attachment of MTs to kinetochores, the model progressively restricts the angle at which binding can occur as more MTs bind (Figure 1E). This is motivated by previous work demonstrating that kinetochore geometry and chromosome rotation play an important role in promoting correct kinetochore-MT attachment and correcting errors [26, 30–33]. We have extended previous work to include both multiple MT binding sites per kinetochore and changes in kinetochore geometry upon binding. In our model, unattached kinetochores have a wide angular range over which attachments can form (modeled as an angular spring constant for binding, represented by the three wide cones in Figure 1E left). Each attachment formed narrows the angle allowed for the subsequent attachment, favoring attachment to MTs that are more perpendicular to the kinetochore plate (represented by the narrower cones in Figure 1E right). Attachments exert an alignment force/torque on kinetochores and MTs based on the stiffness of this angular spring.

To illustrate the importance of progressive restriction, we removed it, making the angular range identical for all three kinetochore-MT attachment events (Figure 4A, Video S4). Doing this nearly abolishes biorientation in the model: the fraction of simulation time for which all three chromosomes are biorienting is below 10%, independent the value of the angular spring constant from 1 $\mathrm{k_B T}$ (almost any angle of attachment is allowed) to 100 $\mathrm{k_B T}$ (attachment is highly restricted in angle). These failures occur for different reasons as the angular spring constant varies. When attachment angle is most permissive, merotelic attachments form and are not corrected sufficiently rapidly to biorient the chromosomes. When the attachment angle is highly restricted, attachments are unlikely to form at all. Overall, this result shows that in our model progressive restriction of attachment is essential for biorientation.

bioRxiv preprint doi: https://doi.org/10.1101/649913; this version posted October 22, 2019. The copyright holder for this preprint (which was not certified by peer review) is the author/funder. All rights reserved. No reuse allowed without permission.

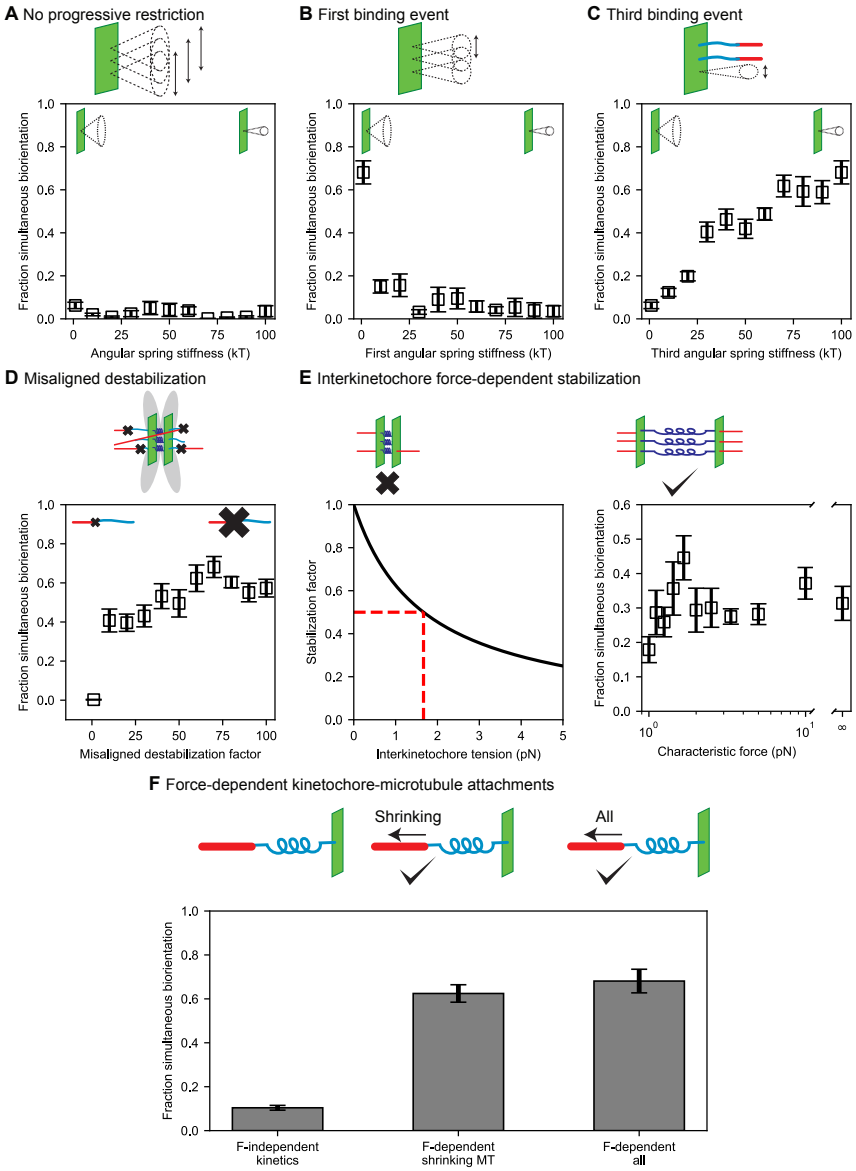

Figure 4: **Results of perturbing kinetochore properties required for biorientation**. **(A)** Fraction simultaneous biorientation versus angular spring stiffness in models lacking progressive restriction of attachment. **(B)** Fraction simultaneous biorientation versus the first angular spring stiffness in the model with progressive restriction. **(C)** Fraction simultaneous biorientation versus the third angular spring stiffness in the model with progressive restriction. **(D)** Fraction simultaneous biorientation versus the misaligned destabilization factor. **(E)** Effects of force-dependent error correction. Top, schematic of stabilization of kinetochore-MT attachments as a function of interkinetochore force. Left, Stabilization as a function of interkinetochore tension for a characteristic force of 1.67 pN. When the interkinetochore force is the characteristic force, attachment turnover is reduced by a factor of two, as shown by the red dashed lines. Right, fraction simultaneous biorientation versus the characteristic force. **(F)** Fraction simultaneous biorientation for different types of force-dependent kinetics (N = 12 simulations per data point).

The progressive restriction model requires that the first binding event be relatively permissive in angle, the second more restricted, and the third highly restricted. To study this, we varied the angular

bioRxiv preprint doi: https://doi.org/10.1101/649913; this version posted October 22, 2019. The copyright holder for this preprint (which was not certified by peer review) is the author/funder. All rights reserved. No reuse allowed without permission.

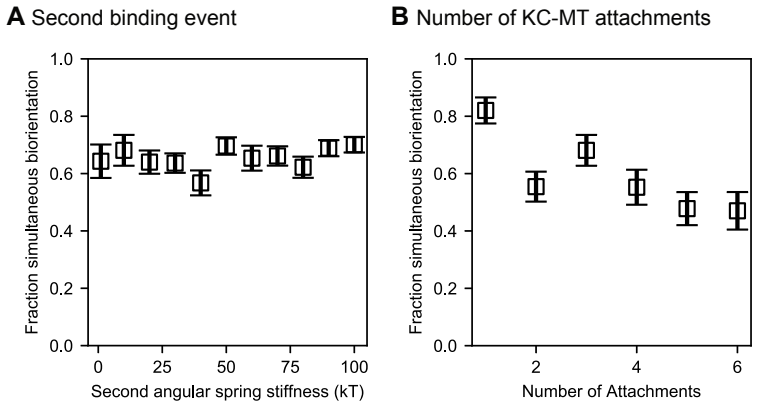

Figure 5: **Figure supplement to figure 4: Effects of varying the middle angular stiffness for progressive restriction and the number of kinetochore-microtubule attachments.** (**A**) Angular spring stiffness for the middle value chosen in progressive restriction did not affect chromosome biorientation fidelity. In these models, the first and third angular spring stiffnesses were fixed at 1 k_BT and 100 k_BT respectively. (**B**) Varying the number of microtubule attachment sites per kinetochore does not significantly alter biorientation in the model. We varied the angular spring stiffnesses are varied with the number of attachments shown as (1: [1 k_BT, 1 k_BT], 2: [1 k_BT, 10 k_BT, 10 k_BT], 3: Reference model, 4–6: [1 k_BT, 10 k_BT, 100 k_BT, 100 k_BT, ... 100 k_BT]) (N = 12 simulations per data point).

spring constant of each attachment independently (Figure 4B,C, Figure 5, Video S4). The model achieves a high fraction of simultaneous biorientation around 70% when the first attachment is maximally permissive (spring constant is 1 $\mathrm{k_BT}$); an increase in this spring constant restricts the angle and decreases simultaneous biorientation to below 20% (Figure 4B). This means that for the first attachment, promoting kinetochore binding to any MT is important: initial attachments should be established easily, even if erroneous. By contrast, biorientation is increased when the third (final) binding event is highly restricted (Figure 4C): chromosomes are bioriented in the model $<$10% of the time when the third attachment is most permissive, but the fraction of simultaneous biorientation increases with the angular stiffness of the third binding site. The second value of the angular potential for progressive restriction was less important (Figure 5A): varying it did not significantly change the fraction of simultaneous biorientation

Because of the importance of progressive restriction in our model, we additionally examined whether varying the number of allowed kinetochore-MT attachments might affect how easily biorientation is achieved, but found no significant effect (Figure 5B). In these simulations, we chose how to vary the angular spring stiffness as the number of attachment sites varies. For fewer attachment sites, we chose the lower values of angular spring stiffnesses for progressive restriction that matched the reference stiffness. For increased number of attachments, the later attachments were fixed at an upper limit of 100 k_BT. In all cases, chromosome biorientation was not compromised.

Error correction occurs through the destabilization of improper attachments

Progressive restriction of attachment reduces but does not eliminate erroneous kinetochore-MT attachments. Previous experimental work has shown that merotelic attachments are common in early mitosis and are corrected over time [119] due to increased turnover of kinetochore MTs from the activity

bioRxiv preprint doi: https://doi.org/10.1101/649913; this version posted October 22, 2019. The copyright holder for this preprint (which was not certified by peer review) is the author/funder. All rights reserved. No reuse allowed without permission.

of Aurora B kinase [41, 105, 109]. To study this, we considered two different error correction models: biorientation-dependent stabilization and force-dependent stabilization. First, we implemented the rule-based model of misaligned destabilization by accelerating the detachment of kinetochore-MT attachments that are not amphitelic (Figure 1F). Because experimental work has demonstrated a decrease in kinetochore MT turnover by up to a factor of 65 in the presence of Aurora B inhibitors [41], we varied the misaligned destabilization factor in the model, which quantifies the increased turnover of incorrect attachments, over a similar range from 1 to 100 (Figure 4D, Video S4). Consistent with experimental results, biorientation is nearly eliminated in the absence of misaligned destabilization. Biorientation time in the model is maximum when the misaligned destabilization factor is 70, comparable to the experimental value. This demonstrates the importance of error correction in the model.

The biorientation-dependent model has the disadvantage that it cannot test any mechanisms by which incorrect attachments are destabilized. We therefore additionally tested a force-dependent error correction model, based on previous results that kinetochore-MT attachments are stabilized by force [120,121]. We modeled the kinetics of kinetochore-MT attachments as a function of interkinetochore tension, with the rates decreasing with force (Figure 4E, Video S5), controlled by a a characteristic force for significant stabilization.

The force-stabilization model of error correction that we implemented experiences the initial problem of biorientation (IPBO): a bioriented attachment that has just formed is not under tension, and therefore is not stable [78, 122, 123]. Consistent with this, we found implementing force-dependent stabilization alone did not lead to biorientation. Recent work has suggested that the IPBO may be solved by initial syntelic-like attachments that are end-on between the kinetochore face near a pole, and lateral to the kinetochore farther from that same pole [38]. Therefore, we varied parameters in the model that might facilitate tension generation before biorientation, including the angular spring constants of the interkinetochore spring, the characteristic angular factor for binding high angles to the kinetochore plate, the effective concentration for binding laterally, and the number of kinesin-5 motors, which affect overall spindle force generation. We were able to achieve long-lived biorientation in the force-dependent error correction model with model parameters that favored end-on over lateral attachments, inhibited attachments at high angle, and allowed sister kinetochores to more easily reorient (Table 6).

In this version of the model, we then varied the characteristic force that controls how much attachments are stabilized by force (Figure 4E, Video S5). The characteristic force is the value of the interkinetochore force at which attachments are stabilized by a factor of two, so a small value reflects rapid variation of attachment stability with force, while an infinite value means that attachments are force independent. We found that the model is sensitive to the value of this characteristic force, with best performance of the model at a characteristic force of 1.67 pN. Higher or lower values decrease cumulative biorientation by up to a factor of two.

Persistent biorientation is achieved through force-dependent kinetochore-microtubule attachment

Once amphitelic kinetochore-MT attachments are formed, they must be maintained for biorientation to persist. Attachments between single MTs and purified budding-yeast kinetochores were altered by force applied to the kinetochore, even in the absence of Aurora kinase [100,101]. In particular, the kinetochore-MT attachment lifetime increased with tension when kinetochores were attached to depolymerizing MTs, an effect dependent on a TOG protein [100,101]. Consistent with this, we implemented force dependence of attachments in the model (Figure 1G). This effect is required to maintain biorientation: if we eliminate

bioRxiv preprint doi: https://doi.org/10.1101/649913; this version posted October 22, 2019. The copyright holder for this preprint (which was not certified by peer review) is the author/funder. All rights reserved. No reuse allowed without permission.

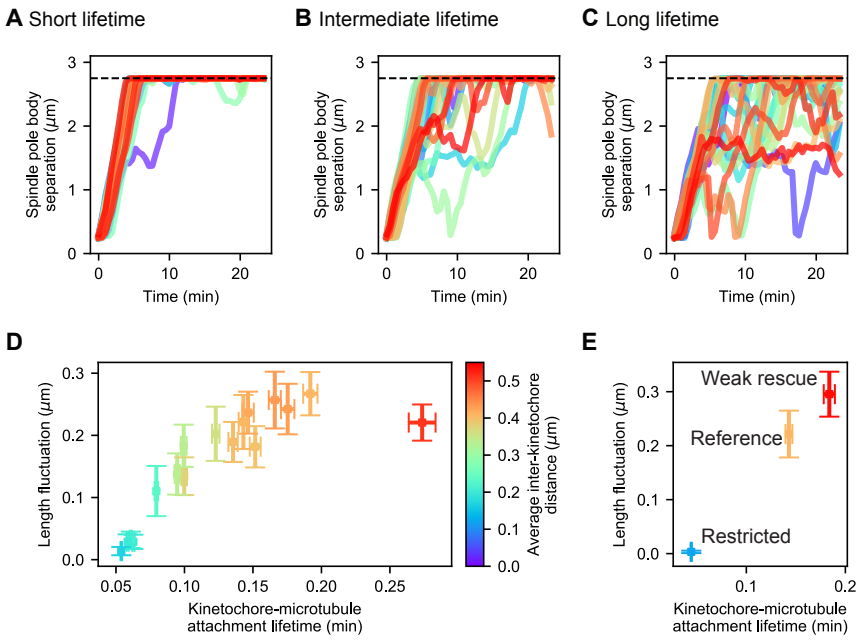

Figure 6: **Changes in kinetochore-MT attachment turnover alter spindle length fluctuations.** **(A-C)** Spindle length versus time for 24 simulations of the same model, with **(A)** short (1/4 the reference value), **(B)** intermediate (1/2 the reference value), and **(C)** long (twice the reference value) kinetochore-MT attachment lifetime. **(D)** Length fluctuation magnitude versus measured kinetochore-MT attachment lifetime and average interkinetochore stretch (color) for bioplar spindles (corresponding to simulation time >10 min.). **(E)** Length fluctuation magnitude versus measured kinetochore-MT attachment lifetime and average interkinetochore stretch (color) for the reference, restricted, and weak rescue models (N = 24 simulations per data point).

the force dependence of attachment kinetics, biorientation is nearly abolished in the model (Figure 4F, Video S4). To understand which force-dependent rate is most important for this effect, we added them back to the model one at a time. The increase in attachment lifetime of a kinetochore bound to a shrinking MT is the key force-dependent rate, because making this the only force-dependent lifetime in the model restores nearly all biorientation compared to the model with all rates force-dependent (Figure 4F). This demonstrates that maintenance of biorientation requires kinetochore-MT attachments to persist during MT depolymerization.

Slow turnover of kinetochore-microtubule attachments can cause spindle length fluctuations

Spindle length regulation [15, 44–47, 50] can be understood using the force-balance model of Saunders and Hoyt in which plus-end directed sliding motors produce outward force, and minus-end directed sliding motors and chromosomes produce inward force [49, 50, 116, 124–132]. The force-balance model has been used in mathematical models of spindles in yeast [15, 51, 59, 63, 65, 66, 133, 134], and *Drosophila* [135–138] cells. This work has focused on spindle length at steady state, not dynamic changes. However, some fission-yeast mutants exhibit large fluctuations in spindle length in which the bipolar spindle assembles, but then shortens or falls apart, known as spindle collapse [50, 52–58]. Re-

bioRxiv preprint doi: https://doi.org/10.1101/649913; this version posted October 22, 2019. The copyright holder for this preprint (which was not certified by peer review) is the author/funder. All rights reserved. No reuse allowed without permission.

markably, fission-yeast double mutants can have wild-type average metaphase spindle length, but much larger fluctuations than wild-type [50]. The underlying mechanisms of large spindle length fluctuations have remained unclear, in part because apparently contradictory changes can cause it. For example, deletion of proteins known either to stabilize [53] or destabilize MTs [52] can both lead to large spindle length fluctuations. In recent work we examined how deletion of the kinesin-8 motor proteins could contribute to large spindle length fluctuations in fission yeast [52], but a general understanding of this phenomenon is unknown. Therefore, we sought to understand what spindle functions might lead to large length fluctuations.

One key determinant of the magnitude of spindle length fluctuations is the lifetime of kinetochore-MT attachments (Figure 6, Video S6). We quantified the magnitude of length fluctuations by determining the standard deviation in spindle length over time after spindle elongation for each individual simulation of the model, then averaging that standard deviation over multiple model runs with the same parameters. This measure of length fluctuations increases with kinetochore-MT attachment lifetime: the longer the lifetime, the larger the fluctuations (Figure 6A-D).

To understand this result, we hypothesized that for long-lived attachment, the force exerted by a stretched kinetochore can grow over time to a larger value: long-lived attachment allows multiple MTs to bind per kinetochore, exert greater force, and stretch apart the sisters. This allows larger inward force to be exerted on the spindle by attached kinetochores. Indeed, the average interkinetochore distance increases with kinetochore-MT attachment lifetime (Figure 6D). Thus, slow cycles of attachment and detachment lead to slowly varying force on the spindle that causes its length to fluctuate. In the opposite limit, short-lived kinetochore-MT attachment causes relatively quick turnover, limiting interkinetochore stretch, inward force, and variation in inward force.

Alteration in kinetochore-MT attachment lifetime could occur through multiple molecular mechanisms. To illustrate how this could occur, we considered two perturbations to the model that have downstream effects on both lifetime and length fluctuations (Figure 6E). The first perturbation is a restricted attachment model, in which the angular spring constant of attachment discussed above (Figure 4A) is set to 100 $\mathrm{k_B T}$ for all attachments. In this case attachments rarely form and when formed, their lifetime is short (< 0.05 min on average). As a result, the force produced by interkinetochore stretch is small and does not vary much, leading to small length fluctuations in the model (< 0.01 μm on average). The opposite limit can occur in a model in which the force-dependent rescue of kinetochore MTs is greatly reduced, by increasing the force constant from 6.4 pN to 12.8 pN (this reduces the force sensitivity of rescue, see Appendix A). This causes kinetochore MTs to depolymerize for longer time, and because kinetochore-MT attachments are stabilized during depolymerization, this change dramatically increases the attachment lifetime to 0.2 min. As a result, interkinetochore stretch can increase, and length fluctuations correspondingly increase (0.2 μm).

This analysis suggests that altered kinetochore-MT attachment lifetime could be a downstream effect that results from some of the diverse mutations observed to cause spindle length in *S. pombe*. We note that the effect of lifetime may not be the only source of spindle length fluctuations: other mutations that lead to slow changes in force exerted on the spindle could have similar effects.

Force generation in the spindle varies during spindle elongation

The force-balance model can explain why multiple perturbations alter steady-state spindle length, including mutation of motors and microtubule-associated proteins [15, 50], and chromosome/kinetochore

bioRxiv preprint doi: https://doi.org/10.1101/649913; this version posted October 22, 2019. The copyright holder for this preprint (which was not certified by peer review) is the author/funder. All rights reserved. No reuse allowed without permission.

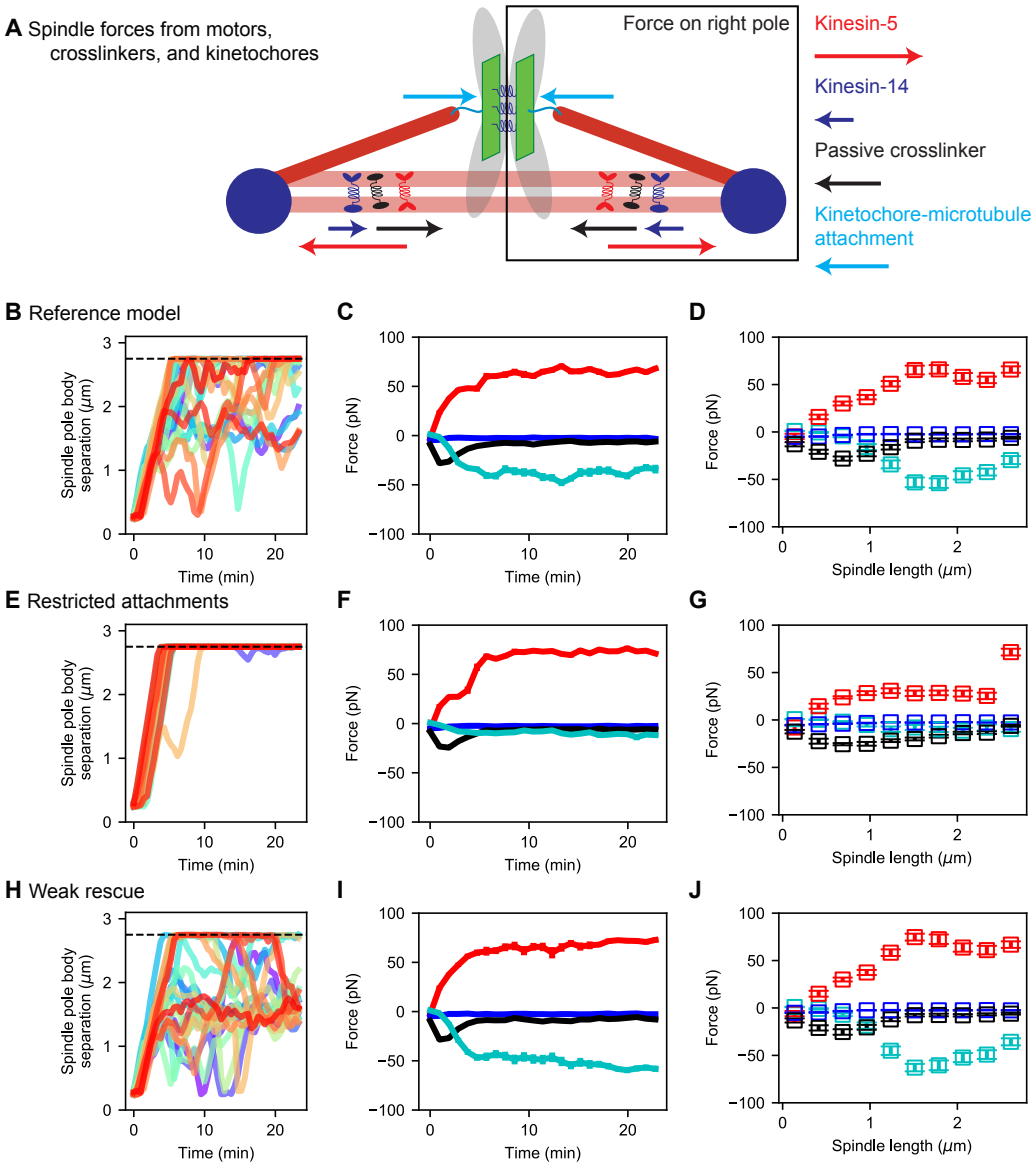

Figure 7: **Spindle force generation varies as the spindle assembles and elongates.** **(A)** Schematic of force generation along the spindle axis, showing kinesin-5 motors exerting outward force (red) and kinesin-14 (dark blue), crosslinkers (black), and kinetochore-MT attachment to stretched chromosomes (light blue) exerting inward force. **(B, E, H)** Spindle length versus time, **(C, F, I)** average spindle axis force versus time, and **(D, G, J)** average spindle axis force versus spindle length for three different models: **(B-D)** the reference model, **(E-G)** the restricted attachment model, and **(H-J)** the weak rescue model (N = 24 simulations per data point).

number and chromatin stiffness [46, 51]. However, it can be challenging to distinguish direct from indirect effects of altering force balance. For example, the force-balance model posits that minus-end-directed kinesin-14 motors contribute inward force that shortens the spindle, so their deletion would be expected to lead to longer spindles. However, in budding yeast, kinesin-14 deletion instead leads to

bioRxiv preprint doi: https://doi.org/10.1101/649913; this version posted October 22, 2019. The copyright holder for this preprint (which was not certified by peer review) is the author/funder. All rights reserved. No reuse allowed without permission.

shorter spindles, because kinesin-14 helps bundle spindle MTs, allowing kinesin-5 motors to generate greater outward force when kinesin-14 is present [15]. Similarly, kinesin-8 deletion in fission yeast leads to longer spindles, but this is likely due to effects of this motor on MT dynamics rather than direct inward force generation by kinesin-8 [50, 52].

To better understand direct and indirect changes in spindle length, we examined the force produced by spindle molecules as the spindle elongates, averaged over many simulation runs (Figure 7, Video S7). In this analysis, we considered each half-spindle separately, and calculated the total force exerted along the spindle axis produced by separate force-generating elements: outward force by kinesin-5 motors, and inward force by kinesin-14 motors, passive crosslinkers, and kinetochore-MT attachments (Figure 7A). We computed spindle length as a function of time (Figure 7B,E,H), force as a function of time (Figure 7C,F,I) and spindle length (Figure 7D,G,J) in the reference, restricted attachment, and weak rescue models.

The early bipolar spindle forms due to motors and crosslinkers, not chromosomes

Force generation by kinesin-5 motors, kinesin-14 motors, crosslinkers, and chromosomes changes significantly as the bipolar spindle assembles. For early time (up to 5 minutes) when spindles are short (up to 1 μm), motors and crosslinkers exert force that slowly increases in magnitde up to a few tens of pN, but chromosomes exert almost no force (Figure 7C,F,I, Video S7). Because chromosomes are not bioriented on the spindle during initial SPB separation, they do not exert significant inward force. This result is consistent with our previous work, which demonstrated that initial bipolar spindle assembly can occur in a model lacking chromosomes [63, 65, 66].

The outward sliding force produced by kinesin-5 motors increases approximately linearly with spindle length, as the length of antiparallel MT overlaps increases during spindle assembly (Figure 7D,G,J). This agrees with the experimental result that the sliding force generated by kinesin-5 motors is proportional to overlap length [139]. The inward force generated by kinesin-14 motors is small, as in previous work that has shown that kinesin-14 is less effective at force generation that kinesin-5 [140] and that in the spindle kinesin-14 may be more important to align spindle MTs than to generate force directly [15].

During initial spindle assembly, crosslinkers play the primary role in maintaining antiparallel MT overlaps in opposition to the sliding activity of kinesin-5. Remarkably, we find that the inward force generated by passive crosslinkers initially increases with spindle length to approximately 25 pN when the spindle is 0.75 μm long. Beyond this point, the crosslinker force steadily decreases, dropping to near zero within a few minutes (Figure 7C,F,I). This is consistent with previous results on force generation by the crosslinker Ase1, which found large force for small overlaps that drops significantly as overlaps become larger [20]. Therefore, our results support a picture of early spindle assembly in which high braking force by crosslinkers on short antiparallel MT overlaps oppose the outward force generated by kinesin-5. This highlights the key role of crosslinkers in early spindle assembly seen previously [63, 65, 66].

Metaphase spindle length is determined primarily by interkinetochore stretch and kinesin-5 motors

Once the spindle elongates sufficiently to separate SPBs by 1 μm, there is a transition in the primary contributer to spindle force. In this regime, chromosomes biorient and the inward force from interkinetochore stretch becomes significant, balancing outward force from kinesin-5 motors (Figure 7C,F,I). This

bioRxiv preprint doi: https://doi.org/10.1101/649913; this version posted October 22, 2019. The copyright holder for this preprint (which was not certified by peer review) is the author/funder. All rights reserved. No reuse allowed without permission.

balance is crucial to setting metaphase spindle length.

To perturb this force balance, we considered two additional models discussed above (Figure 6E) with restricted attachment and weak rescue. When attachment is restricted, chromosomes rarely biorient and the inward force from chromosomes is small for spindles of all length. This leads to unbalanced force from kinesin-5 motors and long spindles (Figure 7E-G, Video S7). When MT rescue is reduced, interkinetochore stretch is larger and the inward force from stretched sister kinetochores increases (Figure 7H-J, Video S7). This leads to shorter metaphase spindle length and a corresponding increase in force from stretched kinetochores.

Chromosome segregation can occur via the same mechanisms that assemble the spindle

After developing the model of spindle assembly and chromosome biorientation, we examined what additional mechanisms were required for the model to segregate chromosomes to the poles. Relatively few changes are required for robust chromosome segregation, suggesting that significant new mechanisms are not required in anaphase for chromosome segregation. The rules added to the model for anaphase A include severing the chromatin spring between kinetochores (based on cumulative time the chromosomes are bioriented), stabilization of kinetochore-MT attachment, and depolymerization of MTs (Table 7). With these additions to the model, simulations consistently segregate chromosomes to the poles (Figure 8A-D, Video S8). We compared our simulations to experimental measurements of chromosome segregation, and found similar speed of chromosome movement to the poles and separation of sisters (Figure 8E-G), as expected from the choice of MT depolymerization speed in the anaphase model.

Discussion

The computational model of mitosis presented here can biorient chromosomes as the spindle assembles. This framework allows us to examine which functions are most important to assemble a bipolar spindle, attach kinetochores to spindle MTs, biorient chromosomes, and segregate them to the poles (Figure 1, Video S1). Our model was refined with experimental data on spindle structure, spindle elongation, and chromosome movements in fission yeast, leading to quantitative agreement with the data (Figure 2, Video S2). The reference model results match previous genetics that found that kinesin-5 motors and CLASP are essential for bipolar spindle assembly [53, 63, 113, 114], which suggests that the model captures key features needed to provide insight into mitotic mechanism.

Three ingredients are required for long-lived biorientation in the model (Figure 4, Video S4). Kinetochores shield themselves from merotely by progressive restriction of attachment. Inclusion of this effect in the model was motivated by recent work on the monopolin complex in fission yeast [30] and attachment-driven compaction of mammalian kinetochores [32]. Progressive restriction has two key effects: it promotes proper attachment by favoring binding of microtubules from the same pole that is already attached to the kinetochore, and simultaneously creates a torque that helps to reorient the kinetochore on the spindle. In previous work, the monopolin complex components Pcs1/Mde4 were found not to be essential in fission yeast [30], but in our model completely removing progressive restriction abolishes biorientation (Figure 4). This suggests the possibility that in fission yeast, other molecules may contribute to progressive restriction in addition to monopolin.

Mimicking the effects of Aurora B kinase by including destabilization of misaligned attachments allows the model to achieve robust error correction. Destabilization by approximately a factor of 70 gives

bioRxiv preprint doi: https://doi.org/10.1101/649913; this version posted October 22, 2019. The copyright holder for this preprint (which was not certified by peer review) is the author/funder. All rights reserved. No reuse allowed without permission.

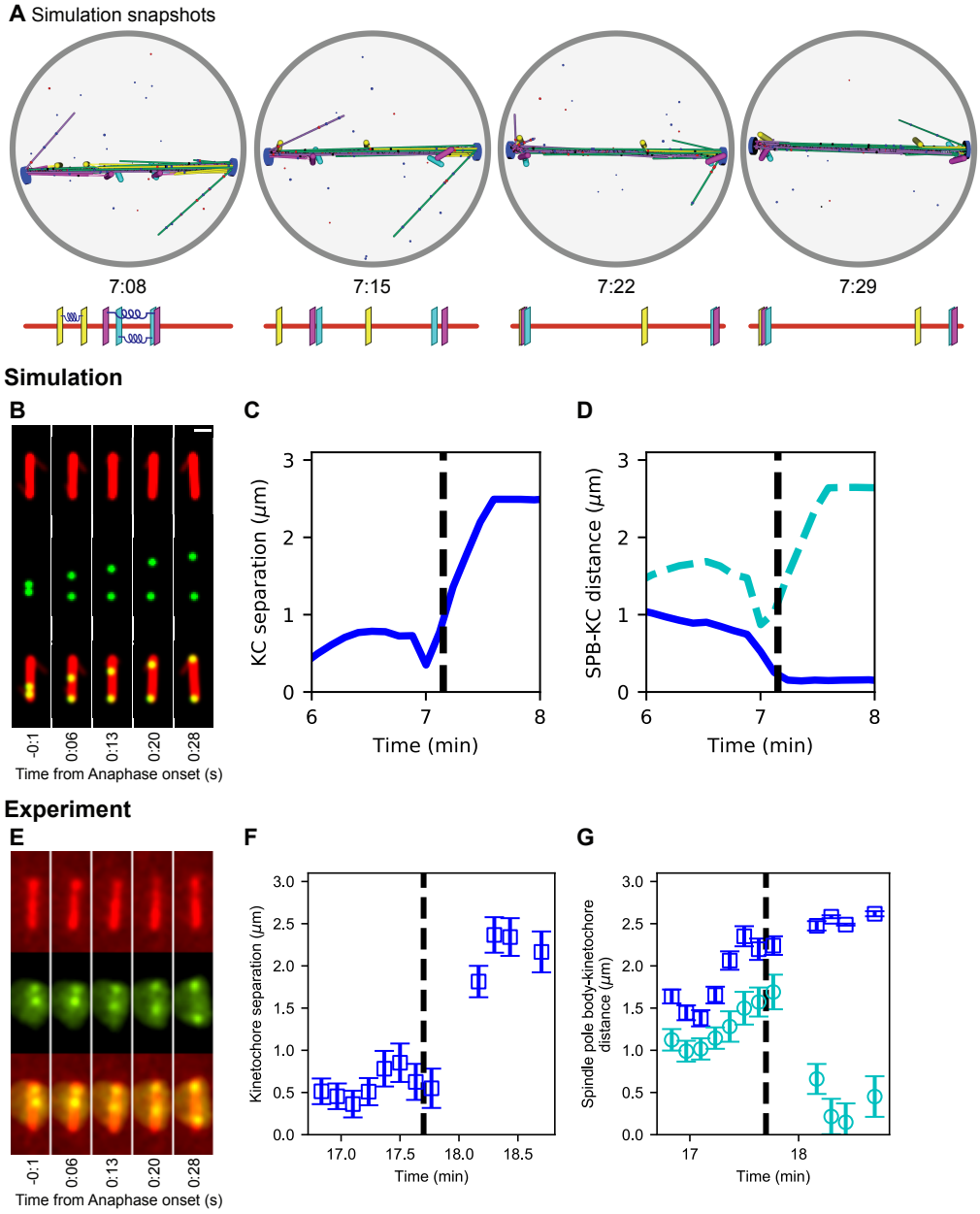

Figure 8: **Chromosome segregation in the model and comparison to experiments**. **(A)** Image sequence of simulation of chromosome segregation after anaphase is triggered, rendered from a three-dimensional simulation. Anaphase begins immediately after the first image. Lower, schematic showing kinetochore position along the spindle. Time shown in minutes:seconds. **(B-D)** Simulation results. **(B)** Simulated fluorescence microscopy images with MTs (red) and a single kinetochore pair (green). Time shown in minutes:seconds. **(C)** Spindle pole body-kinetochore distance, and **(D)** interkinetochore distance versus time from the simulation shown in (B), sampled at a rate comparable to the experimental data in (E-G). **(E-G)** Experimental results. Maximum-intensity projected smoothed images from time-lapse confocal fluorescence microscopy of fission yeast with *mCherry-atb2* labeling MTs (red) and *cen2-GFP* labeling the centromere of chromosome 2 (green). Time shown in minutes:seconds. **(E)** Spindle length, **(F)** spindle pole body-kinetochore distance, and **(G)** interkinetochore distance versus time from the experiment shown in (E).

bioRxiv preprint doi: https://doi.org/10.1101/649913; this version posted October 22, 2019. The copyright holder for this preprint (which was not certified by peer review) is the author/funder. All rights reserved. No reuse allowed without permission.

the highest degree of biorientation the model. This is similar to the degree of destabilization previously estimated to occur due to Aurora B [41], further suggesting that the model produces biologically relevant results.

To maintain long-lived biorientation in the model, kinetochore-MT attachment lifetime must increase with tension during microtubule depolymerization. This catch-bond behavior has been previously measured for purified budding-yeast kinetochores attached to single microtubules [100, 101]. Without this force dependence, kinetochores frequently detach from depolymerizing MTs and lose biorientation. Our model achieves biorientation for the longest time with an increased force-sensitivity of attachment compared to experimental measurements, a difference that would be of interest to explore in future work.

The timing of spindle assembly and biorientation in the model were consistent with those quantified experimentally. A current difference between the model and experiment is that we find ongoing turnover of kinetochore-MT attachments, so that biorientation can be lost once established. This is in contrast to previous experimental work, which suggests that for metaphase spindles, once biorientation is established it is rarely lost [39, 141, 142]. The mechanisms underlying this difference are an open question.

Using our model, we studied the origins of large spindle length fluctuations (Figure 6, Video S6). While previous work has examined regulation of spindle length [15, 46, 47, 50], what mechanisms might drive large fluctuations in spindle length over time have been less well-studied. We identified the lifetime of kinetochore-MT attachment as a determinant of the degree of spindle length fluctuations. Long attachment lifetime allows bioriented chromosomes to become more stretched, leading to large, slowly varying inward force on the spindle. Our results suggest why large spindle length fluctuations have not been seen in larger spindles in vertebrate cells: in *S. pombe*, a relatively small number of kinetochores and MTs contribute to spindle length, and therefore the changing force on the three chromosomes can have a significant effect on the spindle. In vertebrate spindles with tens of thousands of MTs, changes in force on a small number of kinetochores contribute only a small fractional change to overall force on the spindle, leading to smaller fluctuations.

To understand how force generation changes as the spindle assembles, we quantified the force generated by different classes of spindle molecule (Figure 7, Video S7). The early spindle has almost no force generation from interkinetochore stretch because chromosomes are rarely bioriented at this stage. Instead, the early spindle is characterized by outward force from kinesin-5 motors that is resisted by crosslinkers. Consistent with earlier work [20], the force from crosslinkers is highest when MT antiparallel overlaps are short and drops as the spindle elongates. Once the bipolar spindle is formed and chromosomes are bioriented, attached chromosomes provide significant inward force that opposes the outward force of kinesin-5 motors. These results suggest that the many mutations that alter spindle length in fission yeast [50] might act indirectly by altering kinesin-5 force generation or interkinetochore stretch.

Remarkably, the model is able to transition to anaphase A and robustly segregate chromosomes to the poles with a small number of additional rules (Figure 8, Video S8). Overall, our work provides a powerful framework for testing spindle assembly mechanisms that can inform future experimental studies.

bioRxiv preprint doi: https://doi.org/10.1101/649913; this version posted October 22, 2019. The copyright holder for this preprint (which was not certified by peer review) is the author/funder. All rights reserved. No reuse allowed without permission.

Acknowledgments

We thank Jeffrey K. Moore for useful discussions. This work was funded by NSF grants DMR-1725065 (MDB), DMS-1620003 (MAG and MDB), and DMR-1420736 (MAG); NIH grants K25GM110486 (MDB), R01GM124371 (MDB); a fellowship provided by matching funds from the NIH/University of Colorado Biophysics Training Program (AL); and use of the Summit supercomputer, supported by NSF grants ACI-1532235 and ACI-1532236.

References

[1] Wallace F. Marshall. Introduction to Quantitative Cell Biology. Colloquium Series on Quantitative Cell Biology, 3(1):i–50, July 2017.

[2] Alex Mogilner, Roy Wollman, and Wallace F. Marshall. Quantitative Modeling in Cell Biology: What Is It Good for? Developmental Cell, 11(3):279–287, September 2006.

[3] A. Mogilner and E. Craig. Towards a quantitative understanding of mitotic spindle assembly and mechanics. Journal of Cell Science, 123(20):3435–3445, 2010.

[4] Gul Civelekoglu-Scholey and Daniela Cimini. Modelling chromosome dynamics in mitosis: A historical perspective on models of metaphase and anaphase in eukaryotic cells. Interface Focus, 4(3):20130073, June 2014.

[5] Matthew Akamatsu, Julien Berro, Kai-Ming Pu, Irene R. Tebbs, and Thomas D. Pollard. Cytokinetic nodes in fission yeast arise from two distinct types of nodes that merge during interphase. J Cell Biol, 204(6):977–988, March 2014.

[6] Matthew R. Stachowiak, Caroline Laplante, Harvey F. Chin, Boris Guirao, Erdem Karatekin, Thomas D. Pollard, and Ben O'Shaughnessy. Mechanism of Cytokinetic Contractile Ring Constriction in Fission Yeast. Developmental Cell, 29(5):547–561, June 2014.

[7] Jun Allard and Alex Mogilner. Traveling waves in actin dynamics and cell motility. Current opinion in cell biology, 25(1):107–115, February 2013.

[8] Erin L. Barnhart, Jun Allard, Sunny S. Lou, Julie A. Theriot, and Alex Mogilner. Adhesion-Dependent Wave Generation in Crawling Cells. Current Biology, 27(1):27–38, January 2017.

[9] D. Bray. Cell Movements: From Molecules to Motility. Routledge, 2000.

[10] J. Richard McIntosh, Maxim I. Molodtsov, and Fazly I. Ataullakhanov. Biophysics of mitosis. Quarterly Reviews of Biophysics, 45(02):147–207, 2012.

[11] Edwin W. Taylor. Dynamics of Spindle Formation and Its Inhibition by Chemicals. The Journal of Biophysical and Biochemical Cytology, 6(2):193–196, January 1959.

[12] Barbara J. Mann and Patricia Wadsworth. Kinesin-5 Regulation and Function in Mitosis. Trends in Cell Biology, September 2018.

bioRxiv preprint doi: https://doi.org/10.1101/649913; this version posted October 22, 2019. The copyright holder for this preprint (which was not certified by peer review) is the author/funder. All rights reserved. No reuse allowed without permission.

[13] A L Pidoux, M LeDizet, and W Z Cande. Fission yeast pkl1 is a kinesin-related protein involved in mitotic spindle function. Molecular Biology of the Cell, 7(10):1639–1655, October 1996.

[14] Chun Ju Chen, Ken Porche, Ivan Rayment, and Susan P. Gilbert. The ATPase Pathway That Drives the Kinesin-14 Kar3Vik1 Powerstroke. Journal of Biological Chemistry, 287(44):36673–36682, October 2012.

[15] Austin J. Hepperla, Patrick T. Willey, Courtney E. Coombes, Breanna M. Schuster, Maryam Gerami-Nejad, Mark McClellan, Soumya Mukherjee, Janet Fox, Mark Winey, David J. Odde, Eileen O'Toole, and Melissa K. Gardner. Minus-End-Directed Kinesin-14 Motors Align Antiparallel Microtubules to Control Metaphase Spindle Length. Developmental Cell, 31(1):61–72, October 2014.

[16] Christina L. Hueschen, Vahe Galstyan, Meelad Amouzgar, Rob Phillips, and Sophie Dumont. Microtubule End-Clustering Maintains a Steady-State Spindle Shape. Current Biology, 29(4):700–708.e5, February 2019.

[17] Akira Yamashita, Masamitsu Sato, Akiko Fujita, Masayuki Yamamoto, and Takashi Toda. The Roles of Fission Yeast Ase1 in Mitotic Cell Division, Meiotic Nuclear Oscillation, and Cytokinesis Checkpoint Signaling. Molecular Biology of the Cell, 16(3):1378–1395, January 2005.

[18] Marcel E. Janson, Rose Loughlin, Isabelle Loïodice, Chuanhai Fu, Damian Brunner, François J. Nédélec, and Phong T. Tran. Crosslinkers and Motors Organize Dynamic Microtubules to Form Stable Bipolar Arrays in Fission Yeast. Cell, 128(2):357–368, January 2007.

[19] Marcus Braun, Zdenek Lansky, Gero Fink, Felix Ruhnow, Stefan Diez, and Marcel E. Janson. Adaptive braking by Ase1 prevents overlapping microtubules from sliding completely apart. Nature Cell Biology, 13(10):1259–1264, 2011.

[20] Zdenek Lansky, Marcus Braun, Annemarie Lüdecke, Michael Schlierf, Pieter Rein ten Wolde, Marcel E. Janson, and Stefan Diez. Diffusible Crosslinkers Generate Directed Forces in Microtubule Networks. Cell, 160(6):1159–1168, March 2015.

[21] Andrea Musacchio and Arshad Desai. A Molecular View of Kinetochore Assembly and Function. Biology, 6(1):5, January 2017.

[22] Stephen M. Hinshaw and Stephen C. Harrison. Kinetochore Function from the Bottom Up. Trends in Cell Biology, 28(1):22–33, January 2018.

[23] Grace Hamilton, Yoana Dimitrova, and Trisha N. Davis. Seeing is believing: Our evolving view of kinetochore structure, composition, and assembly. Current Opinion in Cell Biology, 60:44–52, October 2019.

[24] Daniela Cimini, Bonnie Howell, Paul Maddox, Alexey Khodjakov, Francesca Degrassi, and E. D. Salmon. Merotelic Kinetochore Orientation Is a Major Mechanism of Aneuploidy in Mitotic Mammalian Tissue Cells. The Journal of Cell Biology, 153(3):517–528, April 2001.

bioRxiv preprint doi: https://doi.org/10.1101/649913; this version posted October 22, 2019. The copyright holder for this preprint (which was not certified by peer review) is the author/funder. All rights reserved. No reuse allowed without permission.

[25] Salmon E.D, Cimini D, Cameron L.A, and DeLuca J.G. Merotelic kinetochores in mammalian tissue cells. Philosophical Transactions of the Royal Society B: Biological Sciences, 360(1455):553–568, March 2005.

[26] Cornelia Rumpf, Lubos Cipak, Alexander Schleiffer, Alison Pidoux, Karl Mechtler, Iva M. Tolić-Nørrelykke, and Juraj Gregan. Laser microsurgery provides evidence for merotelic kinetochore attachments in fission yeast cells lacking Pcs1 or Clr4. Cell Cycle, 9(19):3997–4004, October 2010.

[27] Juraj Gregan, Silvia Polakova, Lijuan Zhang, Iva M. Tolić-Nørrelykke, and Daniela Cimini. Merotelic kinetochore attachment: Causes and effects. Trends in Cell Biology, 21(6):374–381, June 2011.

[28] Michael A. Lampson and Ekaterina L. Grishchuk. Mechanisms to Avoid and Correct Erroneous Kinetochore-Microtubule Attachments. Biology, 6(1):1, January 2017.

[29] Carlos Sacristan and Geert J. P. L. Kops. Joined at the hip: Kinetochores, microtubules, and spindle assembly checkpoint signaling. Trends in Cell Biology, 25(1):21–28, January 2015.

[30] Juraj Gregan, Christian G. Riedel, Alison L. Pidoux, Yuki Katou, Cornelia Rumpf, Alexander Schleiffer, Stephen E. Kearsey, Katsuhiko Shirahige, Robin C. Allshire, and Kim Nasmyth. The Kinetochore Proteins Pcs1 and Mde4 and Heterochromatin Are Required to Prevent Merotelic Orientation. Current Biology, 17(14):1190–1200, July 2007.

[31] R. Paul, R. Wollman, W. T. Silkworth, I. K. Nardi, D. Cimini, and A. Mogilner. Computer simulations predict that chromosome movements and rotations accelerate mitotic spindle assembly without compromising accuracy. Proceedings of the National Academy of Sciences, 106(37):15708–15713, 2009.

[32] Valentin Magidson, Raja Paul, Nachen Yang, Jeffrey G. Ault, Christopher B. O'Connell, Irina Tikhonenko, Bruce F. McEwen, Alex Mogilner, and Alexey Khodjakov. Adaptive changes in the kinetochore architecture facilitate proper spindle assembly. Nature Cell Biology, 2015.

[33] Anatoly V. Zaytsev and Ekaterina L. Grishchuk. Basic mechanism for biorientation of mitotic chromosomes is provided by the kinetochore geometry and indiscriminate turnover of kinetochore microtubules. Molecular Biology of the Cell, 26(22):3985–3998, May 2015.

[34] Andrea Musacchio. The Molecular Biology of Spindle Assembly Checkpoint Signaling Dynamics. Current Biology, 25(20):R1002–R1018, October 2015.

[35] Edward D. Salmon and Kerry Bloom. Tension sensors reveal how the kinetochore shares its load. BioEssays, 39(7):1600216, July 2017.

[36] Natalie J. Nannas and Andrew W. Murray. Tethering Sister Centromeres to Each Other Suggests the Spindle Checkpoint Detects Stretch within the Kinetochore. PLOS Genetics, 10(8):e1004492, August 2014.

bioRxiv preprint doi: https://doi.org/10.1101/649913; this version posted October 22, 2019. The copyright holder for this preprint (which was not certified by peer review) is the author/funder. All rights reserved. No reuse allowed without permission.

[37] Eric C. Tauchman, Frederick J. Boehm, and Jennifer G. DeLuca. Stable kinetochore–microtubule attachment is sufficient to silence the spindle assembly checkpoint in human cells. Nature Communications, 6, December 2015.

[38] Jonathan Kuhn and Sophie Dumont. Spindle assembly checkpoint satisfaction occurs via end-on but not lateral attachments under tension. J Cell Biol, 216(6):1533–1542, June 2017.

[39] Tae Yeon Yoo, Jeong-Mo Choi, William Conway, Che-Hang Yu, Rohit V Pappu, and Daniel J Needleman. Measuring NDC80 binding reveals the molecular basis of tension-dependent kinetochore-microtubule attachments. eLife, 7:e36392, July 2018.

[40] Iain M. Cheeseman, Scott Anderson, Miri Jwa, Erin M. Green, Jung-seog Kang, John R. Yates III, Clarence S. M. Chan, David G. Drubin, and Georjana Barnes. Phospho-Regulation of Kinetochore-Microtubule Attachments by the Aurora Kinase Ipl1p. Cell, 111(2):163–172, October 2002.

[41] Daniela Cimini, Xiaohu Wan, Christophe B. Hirel, and E. D. Salmon. Aurora Kinase Promotes Turnover of Kinetochore Microtubules to Reduce Chromosome Segregation Errors. Current Biology, 16(17):1711–1718, September 2006.

[42] Dan Liu, Gerben Vader, Martijn J. M. Vromans, Michael A. Lampson, and Susanne M. A. Lens. Sensing chromosome bi-orientation by spatial separation of aurora B kinase from kinetochore substrates. Science (New York, N.Y.), 323(5919):1350–1353, March 2009.

[43] Dan Liu, Mathijs Vleugel, Chelsea B. Backer, Tetsuya Hori, Tatsuo Fukagawa, Iain M. Cheeseman, and Michael A. Lampson. Regulated targeting of protein phosphatase 1 to the outer kinetochore by KNL1 opposes Aurora B kinase. The Journal of Cell Biology, page jcb.201001006, March 2010.

[44] Sophie Dumont and Timothy J. Mitchison. Force and Length in the Mitotic Spindle. Current Biology, 19(17):R749–R761, September 2009.

[45] Gohta Goshima and Jonathan M. Scholey. Control of Mitotic Spindle Length. Annual Review of Cell and Developmental Biology, 26(1):21–57, 2010.

[46] Natalie J. Nannas, Eileen T. O'Toole, Mark Winey, and Andrew W. Murray. Chromosomal attachments set length and microtubule number in the Saccharomyces cerevisiae mitotic spindle. Molecular Biology of the Cell, 25(25):4034–4048, December 2014.

[47] Rania S. Rizk, Katherine A. DiScipio, Kathleen G. Proudfoot, and Mohan L. Gupta. The kinesin-8 Kip3 scales anaphase spindle length by suppression of midzone microtubule polymerization. The Journal of Cell Biology, 204(6):965–975, March 2014.

[48] Benjamin Lacroix, Gaëlle Letort, Laras Pitayu, Jérémy Sallé, Marine Stefanutti, Gilliane Maton, Anne-Marie Ladouceur, Julie C. Canman, Paul S. Maddox, Amy S. Maddox, Nicolas Minc, François Nédélec, and Julien Dumont. Microtubule Dynamics Scale with Cell Size to Set Spindle Length and Assembly Timing. Developmental Cell, 45(4):496–511.e6, May 2018.

bioRxiv preprint doi: https://doi.org/10.1101/649913; this version posted October 22, 2019. The copyright holder for this preprint (which was not certified by peer review) is the author/funder. All rights reserved. No reuse allowed without permission.

[49] William S. Saunders and M. Andrew Hoyt. Kinesin-related proteins required for structural integrity of the mitotic spindle. Cell, 70(3):451–458, August 1992.

[50] Viktoriya Syrovatkina, Chuanhai Fu, and Phong T. Tran. Antagonistic Spindle Motors and MAPs Regulate Metaphase Spindle Length and Chromosome Segregation. Current Biology, 23(23):2423–2429, December 2013.

[51] Jeremy M. Chacón, Soumya Mukherjee, Breanna M. Schuster, Duncan J. Clarke, and Melissa K. Gardner. Pericentromere tension is self-regulated by spindle structure in metaphase. The Journal of Cell Biology, 205(3):313–324, December 2014.

[52] Zachary R. Gergely, Ammon Crapo, Loren E. Hough, J. Richard McIntosh, and Meredith D. Betterton. Kinesin-8 effects on mitotic microtubule dynamics contribute to spindle function in fission yeast. Molecular Biology of the Cell, 27(22):3490–3514, July 2016.

[53] Scott V. Bratman and Fred Chang. Stabilization of Overlapping Microtubules by Fission Yeast CLASP. Developmental Cell, 13(6):812–827, December 2007.

[54] Karen Griffiths, Hirohisa Masuda, Susheela Dhut, and Takashi Toda. Fission yeast dam1-A8 mutant is resistant to and rescued by an anti-microtubule agent. Biochemical and Biophysical Research Communications, 368(3):670–676, April 2008.

[55] Sung Hugh Choi, Marie-Pierre Péli-Gulli, Iain Mcleod, Ali Sarkeshik, John R. Yates, Viesturs Simanis, and Dannel McCollum. Phosphorylation state defines discrete roles for monopolin in chromosome attachment and spindle elongation. Current biology: CB, 19(12):985–995, June 2009.

[56] Kuo-Shun Hsu and Takashi Toda. Ndc80 Internal Loop Interacts with Dis1/TOG to Ensure Proper Kinetochore-Spindle Attachment in Fission Yeast. Current Biology, 21(3):214–220, February 2011.

[57] Hirohisa Masuda, Risa Mori, Masashi Yukawa, and Takashi Toda. Fission yeast MOZART1/Mzt1 is an essential γ-tubulin complex component required for complex recruitment to the microtubule organizing center, but not its assembly. Molecular Biology of the Cell, 24(18):2894–2906, September 2013.

[58] Sarah Wälde and Megan C. King. The KASH protein Kms2 coordinates mitotic remodeling of the spindle pole body. J Cell Sci, 127(16):3625–3640, August 2014.

[59] Jonathan J. Ward, Hélio Roque, Claude Antony, and François Nédélec. Mechanical design principles of a mitotic spindle. eLife, 3:e03398, January 2015.

[60] Hadrien Mary, Jonathan Fouchard, Guillaume Gay, Céline Reyes, Tiphaine Gauthier, Clémence Gruget, Jacques Pécréaux, Sylvie Tournier, and Yannick Gachet. Fission yeast kinesin-8 controls chromosome congression independently of oscillations. J Cell Sci, 128(20):3720–3730, October 2015.

bioRxiv preprint doi: https://doi.org/10.1101/649913; this version posted October 22, 2019. The copyright holder for this preprint (which was not certified by peer review) is the author/funder. All rights reserved. No reuse allowed without permission.

[61] Anna H. Klemm, Agneza Bosilj, Matko Gluncic, Nenad Pavin, and Iva M. Tolic. Metaphase kinetochore movements are regulated by kinesin-8 motors and microtubule dynamic instability. Molecular Biology of the Cell, 29(11):1332–1345, April 2018.

[62] Robert Blackwell, Oliver Sweezy-Schindler, Christopher Edelmaier, Zachary R. Gergely, Patrick J. Flynn, Salvador Montes, Ammon Crapo, Alireza Doostan, J. Richard McIntosh, Matthew A. Glaser, and Meredith D. Betterton. Contributions of Microtubule Dynamic Instability and Rotational Diffusion to Kinetochore Capture. Biophysical Journal, 112(3):552–563, February 2017.

[63] Robert Blackwell, Christopher Edelmaier, Oliver Sweezy-Schindler, Adam Lamson, Zachary R. Gergely, Eileen O'Toole, Ammon Crapo, Loren E. Hough, J. Richard McIntosh, Matthew A. Glaser, and Meredith D. Betterton. Physical determinants of bipolar mitotic spindle assembly and stability in fission yeast. Science Advances, 3(1):e1601603, January 2017.

[64] Matko Glunčić, Nicola Maghelli, Alexander Krull, Vladimir Krstić, Damien Ramunno-Johnson, Nenad Pavin, and Iva M. Tolić. Kinesin-8 Motors Improve Nuclear Centering by Promoting Microtubule Catastrophe. Physical Review Letters, 114(7):078103, February 2015.

[65] Adam R. Lamson, Christopher J. Edelmaier, Matthew A. Glaser, and Meredith D. Betterton. Theory of Cytoskeletal Reorganization during Cross-Linker-Mediated Mitotic Spindle Assembly. Biophysical Journal, 116(9):1719–1731, May 2019.

[66] Sergio A. Rincon, Adam Lamson, Robert Blackwell, Viktoriya Syrovatkina, Vincent Fraisier, Anne Paoletti, Meredith D. Betterton, and Phong T. Tran. Kinesin-5-independent mitotic spindle assembly requires the antiparallel microtubule crosslinker Ase1 in fission yeast. Nature Communications, 8:15286, May 2017.

[67] Elina Vladimirou, Ed Harry, Nigel Burroughs, and Andrew D. McAinsh. Springs, clutches and motors: Driving forward kinetochore mechanism by modelling. Chromosome Research, 19(3):409–421, February 2011.

[68] Ingrid Brust-Mascher, Gul Civelekoglu-Scholey, and Jonathan M. Scholey. Mechanism for Anaphase B: Evaluation of "Slide-and-Cluster" versus "Slide-and-Flux-or-Elongate" Models. Biophysical Journal, 108(8):2007–2018, April 2015.

[69] D. Johann, D. Goswami, and K. Kruse. Generation of Stable Overlaps between Antiparallel Filaments. Physical Review Letters, 115(11):118103, September 2015.

[70] D. Johann, D. Goswami, and K. Kruse. Assembly of bipolar microtubule structures by passive cross-linkers and molecular motors. Physical Review E, 93(6):062415, June 2016.

[71] Rui Ma, Liedewij Laan, Marileen Dogterom, Nenad Pavin, and Frank Jülicher. General theory for the mechanics of confined microtubule asters. New Journal of Physics, 16(1):013018, January 2014.

[72] Carlos Garzon-Coral, Horatiu A. Fantana, and Jonathon Howard. A force-generating machinery maintains the spindle at the cell center during mitosis. Science, 352(6289):1124–1127, May 2016.

bioRxiv preprint doi: https://doi.org/10.1101/649913; this version posted October 22, 2019. The copyright holder for this preprint (which was not certified by peer review) is the author/funder. All rights reserved. No reuse allowed without permission.

[73] Jan Brugués and Daniel Needleman. Physical basis of spindle self-organization. Proceedings of the National Academy of Sciences, 111(52):18496–18500, December 2014.

[74] Maja Novak, Bruno Polak, Juraj Simunić, Zvonimir Boban, Barbara Kuzmić, Andreas W. Thomae, Iva M. Tolić, and Nenad Pavin. The mitotic spindle is chiral due to torques within microtubule bundles. Nature Communications, 9(1):3571, September 2018.

[75] Stefanie Redemann, Johannes Baumgart, Norbert Lindow, Michael Shelley, Ehssan Nazockdast, Andrea Kratz, Steffen Prohaska, Jan Brugués, Sebastian Fürthauer, and Thomas Müller-Reichert. C. elegans chromosomes connect to centrosomes by anchoring into the spindle network. Nature Communications, 8:15288, May 2017.

[76] Lora Winters, Ivana Ban, Marcel Prelogović, Iana Kalinina, Nenad Pavin, and Iva M. Tolić. Pivoting of microtubules driven by minus-end-directed motors leads to spindle assembly. BMC Biology, 17(1):42, May 2019.

[77] Iana Kalinina, Amitabha Nandi, Petrina Delivani, Mariola R. Chacón, Anna H. Klemm, Damien Ramunno-Johnson, Alexander Krull, Benjamin Lindner, Nenad Pavin, and Iva M. Tolić-Norrelykke. Pivoting of microtubules around the spindle pole accelerates kinetochore capture. Nature Cell Biology, 2012.

[78] Emily S. Tubman, Sue Biggins, and David J. Odde. Stochastic Modeling Yields a Mechanistic Framework for Spindle Attachment Error Correction in Budding Yeast Mitosis. Cell Systems, 4(6):645–650.e5, June 2017.

[79] Prasad Trivedi, Anatoly V. Zaytsev, Maxim Godzi, Fazly I. Ataullakhanov, Ekaterina L. Grishchuk, and P. Todd Stukenberg. The binding of Borealin to microtubules underlies a tension independent kinetochore-microtubule error correction pathway. Nature Communications, 10(1):682, February 2019.

[80] Jonathan W. Armond, Edward F. Harry, Andrew D. McAinsh, and Nigel J. Burroughs. Inferring the Forces Controlling Metaphase Kinetochore Oscillations by Reverse Engineering System Dynamics. PLOS Computational Biology, 11(11):e1004607, November 2015.

[81] Edward J. Banigan, Kevin K. Chiou, Edward R. Ballister, Alyssa M. Mayo, Michael A. Lampson, and Andrea J. Liu. Minimal model for collective kinetochore–microtubule dynamics. Proceedings of the National Academy of Sciences, 112(41):12699–12704, October 2015.

[82] Kruno Vukušić, Renata Buđa, Agneza Bosilj, Ana Milas, Nenad Pavin, and Iva M. Tolić. Microtubule Sliding within the Bridging Fiber Pushes Kinetochore Fibers Apart to Segregate Chromosomes. Developmental Cell, 43(1):11–23.e6, October 2017.

[83] Tong Gao, Robert Blackwell, Matthew A. Glaser, Meredith Betterton, and Michael J. Shelley. Multiscale Polar Theory of Microtubule and Motor-Protein Assemblies. Physical Review Letters, 114(4):048101, January 2015.

[84] Tong Gao, Robert Blackwell, Matthew A. Glaser, M. D. Betterton, and Michael J. Shelley. Multiscale modeling and simulation of microtubule-motor-protein assemblies. Physical Review E, 92(6):062709, December 2015.

bioRxiv preprint doi: https://doi.org/10.1101/649913; this version posted October 22, 2019. The copyright holder for this preprint (which was not certified by peer review) is the author/funder. All rights reserved. No reuse allowed without permission.

[85] Robert Blackwell, Oliver Sweezy-Schindler, Christopher Baldwin, Loren E. Hough, Matthew A. Glaser, and M. D. Betterton. Microscopic origins of anisotropic active stress in motor-driven nematic liquid crystals. Soft Matter, 12:2676–2687, January 2016.

[86] Masaki Edamatsu. Bidirectional motility of the fission yeast kinesin-5, Cut7. Biochemical and Biophysical Research Communications, 446(1):231–234, March 2014.

[87] M. Edamatsu. Molecular properties of the N-terminal extension of the fission yeast kinesin-5, Cut7. Genetics and molecular research : GMR, 15(1), February 2016.

[88] Mishan Britto, Adeline Goulet, Syeda Rizvi, Ottilie von Loeffelholz, Carolyn A. Moores, and Robert A. Cross. Schizosaccharomyces pombe kinesin-5 switches direction using a steric blocking mechanism. Proceedings of the National Academy of Sciences, page 201611581, November 2016.

[89] Sudhir Kumar Singh, Himanshu Pandey, Jawdat Al-Bassam, and Larisa Gheber. Bidirectional motility of kinesin-5 motor proteins: Structural determinants, cumulative functions and physiological roles. Cellular and Molecular Life Sciences, 75(10):1757–1771, May 2018.

[90] Cynthia L. Troxell, Mark A. Sweezy, Robert R. West, Karen D. Reed, Bryan D. Carson, Alison L. Pidoux, W. Zacheus Cande, and J. Richard McIntosh. Pkl1 +andklp2 +: Two Kinesins of the Kar3 Subfamily in Fission Yeast Perform Different Functions in Both Mitosis and Meiosis. Molecular Biology of the Cell, 12(11):3476–3488, January 2001.

[91] Zachary T. Olmsted, Andrew G. Colliver, Timothy D. Riehlman, and Janet L. Paluh. Kinesin-14 and kinesin-5 antagonistically regulate microtubule nucleation by γ-TuRC in yeast and human cells. Nature Communications, 5:5339, October 2014.

[92] Masashi Yukawa, Chiho Ikebe, and Takashi Toda. The Msd1–Wdr8–Pkl1 complex anchors microtubule minus ends to fission yeast spindle pole bodies. J Cell Biol, 209(4):549–562, May 2015.

[93] Masashi Yukawa, Yusuke Yamada, Tomoaki Yamauchi, and Takashi Toda. Two spatially distinct Kinesin-14 Pkl1 and Klp2 generate collaborative inward forces against Kinesin-5 Cut7 in S. pombe. J Cell Sci, page jcs.210740, January 2017.

[94] Isabelle Loïodice, Jayme Staub, Thanuja Gangi Setty, Nam-Phuong T. Nguyen, Anne Paoletti, and P. T. Tran. Ase1p Organizes Antiparallel Microtubule Arrays during Interphase and Mitosis in Fission Yeast. Molecular Biology of the Cell, 16(4):1756–1768, January 2005.

[95] Lukas C. Kapitein, Marcel E. Janson, Siet M. J. L. van den Wildenberg, Casper C. Hoogenraad, Christoph F. Schmidt, and Erwin J. G. Peterman. Microtubule-Driven Multimerization Recruits ase1p onto Overlapping Microtubules. Current Biology, 18(21):1713–1717, November 2008.

[96] Thibault Courtheoux, Guillaume Gay, Yannick Gachet, and Sylvie Tournier. Ase1/Prc1-dependent spindle elongation corrects merotely during anaphase in fission yeast. The Journal of Cell Biology, 187(3):399–412, February 2009.

[97] Chuanhai Fu, Jonathan J. Ward, Isabelle Loiodice, Guilhem Velve-Casquillas, Francois J. Nedelec, and Phong T. Tran. Phospho-Regulated Interaction between Kinesin-6 Klp9p and Microtubule Bundler Ase1p Promotes Spindle Elongation. Developmental Cell, 17(2):257–267, August 2009.

bioRxiv preprint doi: https://doi.org/10.1101/649913; this version posted October 22, 2019. The copyright holder for this preprint (which was not certified by peer review) is the author/funder. All rights reserved. No reuse allowed without permission.

[98] R. Ding, K. L. McDonald, and J. R. McIntosh. Three-dimensional reconstruction and analysis of mitotic spindles from the yeast, Schizosaccharomyces pombe. The Journal of Cell Biology, 120(1):141–151, January 1993.

[99] Takashi Akera, Yuhei Goto, Masamitsu Sato, Masayuki Yamamoto, and Yoshinori Watanabe. Mad1 promotes chromosome congression by anchoring a kinesin motor to the kinetochore. Nature Cell Biology, 17(9):1124–1133, September 2015.

[100] Bungo Akiyoshi, Krishna K. Sarangapani, Andrew F. Powers, Christian R. Nelson, Steve L. Reichow, Hugo Arellano-Santoyo, Tamir Gonen, Jeffrey A. Ranish, Charles L. Asbury, and Sue Biggins. Tension directly stabilizes reconstituted kinetochore-microtubule attachments. Nature, 468(7323):576–579, November 2010.

[101] Matthew P. Miller, Charles L. Asbury, and Sue Biggins. A TOG Protein Confers Tension Sensitivity to Kinetochore-Microtubule Attachments. Cell, 165(6):1428–1439, June 2016.

[102] Chris A. Smith, Andrew D. McAinsh, and Nigel J. Burroughs. Human kinetochores are swivel joints that mediate microtubule attachments. eLife, 5:e16159, September 2016.

[103] Y. Yamagishi, C. H. Yang, Y. Tanno, and Y. Watanabe. MPS1/Mph1 phosphorylates the kinetochore protein KNL1/Spc7 to recruit SAC components. Nature Cell Biology, 14(7):746–752, 2012.

[104] Ayumu Yamamoto and Yasushi Hiraoka. Monopolar spindle attachment of sister chromatids is ensured by two distinct mechanisms at the first meiotic division in fission yeast. The EMBO Journal, 22(9):2284–2296, May 2003.

[105] Guillaume Gay, Thibault Courtheoux, Céline Reyes, Sylvie Tournier, and Yannick Gachet. A stochastic model of kinetochore–microtubule attachment accurately describes fission yeast chromosome segregation. The Journal of Cell Biology, 196(6):757–774, March 2012.

[106] Khuloud Jaqaman, Dinah Loerke, Marcel Mettlen, Hirotaka Kuwata, Sergio Grinstein, Sandra L. Schmid, and Gaudenz Danuser. Robust single-particle tracking in live-cell time-lapse sequences. Nature Methods, 5(8):695–702, August 2008.

[107] E. L. Grishchuk and J. R. McIntosh. Microtubule depolymerization can drive poleward chromosome motion in fission yeast. The EMBO Journal, 25(20):4888–4896, 2006.

[108] J. Richard McIntosh, Eileen O'Toole, Kirill Zhudenkov, Mary Morphew, Cindi Schwartz, Fazly I. Ataullakhanov, and Ekaterina L. Grishchuk. Conserved and divergent features of kinetochores and spindle microtubule ends from five species. The Journal of Cell Biology, 200(4):459–474, February 2013.

[109] Jennifer G. DeLuca, Walter E. Gall, Claudio Ciferri, Daniela Cimini, Andrea Musacchio, and E. D. Salmon. Kinetochore Microtubule Dynamics and Attachment Stability Are Regulated by Hec1. Cell, 127(5):969–982, December 2006.

bioRxiv preprint doi: https://doi.org/10.1101/649913; this version posted October 22, 2019. The copyright holder for this preprint (which was not certified by peer review) is the author/funder. All rights reserved. No reuse allowed without permission.

[110] A. Franco, J. C. Meadows, and J. B. A. Millar. The Dam1/DASH complex is required for the retrieval of unclustered kinetochores in fission yeast. Journal of Cell Science, 120(19):3345–3351, 2007.

[111] Yannick Gachet, Céline Reyes, Thibault Courthéoux, Sherilyn Goldstone, Guillaume Gay, Céline Serrurier, and Sylvie Tournier. Sister Kinetochore Recapture in Fission Yeast Occurs by Two Distinct Mechanisms, Both Requiring Dam1 and Klp2. Molecular Biology of the Cell, 19(4):1646–1662, January 2008.

[112] Qi Gao, Thibault Courtheoux, Yannick Gachet, Sylvie Tournier, and Xiangwei He. A non-ring-like form of the Dam1 complex modulates microtubule dynamics in fission yeast. Proceedings of the National Academy of Sciences, 107(30):13330–13335, July 2010.

[113] Iain Hagan and Mitsuhiro Yanagida. Novel potential mitotic motor protein encoded by the fission yeast cut7+ gene. Nature, 347(6293):563–566, October 1990.

[114] Iain Hagan and Mitsuhiro Yanagida. Kinesin-related cut 7 protein associates with mitotic and meiotic spindles in fission yeast. Nature, 356(6364):74, March 1992.

[115] Takashi Toda, Masashi Yukawa, and Yusuke Yamada. Suppressor analysis uncovers that MAPs and microtubule dynamics balance with the Cut7/Kinesin-5 motor for mitotic spindle assembly in Schizosaccharomyces pombe. bioRxiv, page 380493, July 2018.

[116] Viktoriya Syrovatkina and Phong T. Tran. Loss of kinesin-14 results in aneuploidy via kinesin-5-dependent microtubule protrusions leading to chromosome cut. Nature Communications, 6:7322, June 2015.

[117] Masashi Yukawa, Masaki Okazaki, Yasuhiro Teratani, Ken'ya Furuta, and Takashi Toda. Kinesin-6 Klp9 plays motor-dependent and -independent roles in collaboration with Kinesin-5 Cut7 and the microtubule crosslinker Ase1 in fission yeast. Scientific Reports, 9(1):7336, May 2019.

[118] Alejandro Carpy, Karsten Krug, Sabine Graf, André Koch, Sasa Popic, Silke Hauf, and Boris Macek. Absolute Proteome and Phosphoproteome Dynamics during the Cell Cycle of Schizosaccharomyces pombe (Fission Yeast). Molecular & Cellular Proteomics, 13(8):1925–1936, January 2014.

[119] Daniela Cimini, Ben Moree, Julie C. Canman, and E. D. Salmon. Merotelic kinetochore orientation occurs frequently during early mitosis in mammalian tissue cells and error correction is achieved by two different mechanisms. Journal of Cell Science, 116(20):4213–4225, October 2003.

[120] R. Bruce Nicklas and Carol A. Koch. CHROMOSOME MICROMANIPULATION: III. Spindle Fiber Tension and the Reorientation of Mal-Oriented Chromosomes. The Journal of Cell Biology, 43(1):40–50, October 1969.

[121] Stuart Cane, Anna A. Ye, Sasha J. Luks-Morgan, and Thomas J. Maresca. Elevated polar ejection forces stabilize kinetochore–microtubule attachments. J Cell Biol, 200(2):203–218, January 2013.

bioRxiv preprint doi: https://doi.org/10.1101/649913; this version posted October 22, 2019. The copyright holder for this preprint (which was not certified by peer review) is the author/funder. All rights reserved. No reuse allowed without permission.

[122] Tongli Zhang, Raquel A. Oliveira, Bernhard Schmierer, and Béla Novák. Dynamical Scenarios for Chromosome Bi-orientation. Biophysical Journal, 104(12):2595–2606, June 2013.

[123] Maria Kalantzaki, Etsushi Kitamura, Tongli Zhang, Akihisa Mino, Béla Novák, and Tomoyuki U. Tanaka. Kinetochore–microtubule error correction is driven by differentially regulated interaction modes. Nature Cell Biology, 17(4):421–433, April 2015.

[124] Kentaro Nabeshima, Takashi Nakagawa, Aaron F. Straight, Andrew Murray, Yuji Chikashige, Yukiko M. Yamashita, Yasushi Hiraoka, and Mitsuhiro Yanagida. Dynamics of Centromeres during Metaphase–Anaphase Transition in Fission Yeast: Dis1 Is Implicated in Force Balance in Metaphase Bipolar Spindle. Molecular Biology of the Cell, 9(11):3211–3225, January 1998.

[125] Gohta Goshima, Shigeaki Saitoh, and Mitsuhiro Yanagida. Proper metaphase spindle length is determined by centromere proteins Mis12 and Mis6 required for faithful chromosome segregation. Genes & Development, 13(13):1664–1677, January 1999.

[126] Fedor Severin, Bianca Habermann, Tim Huffaker, and Tony Hyman. Stu2 Promotes Mitotic Spindle Elongation in Anaphase. The Journal of Cell Biology, 153(2):435–442, April 2001.

[127] Iva Marija Tolić-Nørrelykke, Emilia-Laura Munteanu, Genevieve Thon, Lene Oddershede, and Kirstine Berg-Sørensen. Anomalous Diffusion in Living Yeast Cells. Physical Review Letters, 93(7):078102, August 2004.

[128] David C. Bouck and Kerry Bloom. Pericentric Chromatin Is an Elastic Component of the Mitotic Spindle. Current Biology, 17(9):741–748, May 2007.

[129] Andrew D. Stephens, Rachel A. Haggerty, Paula A. Vasquez, Leandra Vicci, Chloe E. Snider, Fu Shi, Cory Quammen, Christopher Mullins, Julian Haase, Russell M. Taylor, Jolien S. Verdaasdonk, Michael R. Falvo, Yuan Jin, M. Gregory Forest, and Kerry Bloom. Pericentric chromatin loops function as a nonlinear spring in mitotic force balance. The Journal of Cell Biology, 200(6):757–772, March 2013.

[130] Judite Costa, Chuanhai Fu, V. Mohini Khare, and Phong T. Tran. Csi2p modulates microtubule dynamics and organizes the bipolar spindle for chromosome segregation. Molecular Biology of the Cell, pages mbc.E14–09–1370, September 2014.

[131] Fan Zheng, Tianpeng Li, Dong-yan Jin, Viktoriya Syrovatkina, Kathleen Scheffler, Phong T. Tran, and Chuanhai Fu. Csi1p recruits alp7p/TACC to the spindle pole bodies for bipolar spindle formation. Molecular Biology of the Cell, 25(18):2750–2760, September 2014.

[132] Roy G. H. P. van Heesbeen, Marvin E. Tanenbaum, and René H. Medema. Balanced Activity of Three Mitotic Motors Is Required for Bipolar Spindle Assembly and Chromosome Segregation. Cell Reports, 8(4):948–956, August 2014.

[133] Melissa K. Gardner, Chad G. Pearson, Brian L. Sprague, Ted R. Zarzar, Kerry Bloom, E. D. Salmon, and David J. Odde. Tension-dependent Regulation of Microtubule Dynamics at Kinetochores Can Explain Metaphase Congression in Yeast. Molecular Biology of the Cell, 16(8):3764–3775, January 2005.

bioRxiv preprint doi: https://doi.org/10.1101/649913; this version posted October 22, 2019. The copyright holder for this preprint (which was not certified by peer review) is the author/funder. All rights reserved. No reuse allowed without permission.

[134] Melissa K. Gardner, David J. Odde, and Kerry Bloom. Kinesin-8 molecular motors: Putting the brakes on chromosome oscillations. Trends in Cell Biology, 18(7):307–310, July 2008.

[135] E.N. Cytrynbaum, J.M. Scholey, and A. Mogilner. A Force Balance Model of Early Spindle Pole Separation in Drosophila Embryos. Biophysical Journal, 84(2):757–769, February 2003.

[136] E. N. Cytrynbaum, P. Sommi, I. Brust-Mascher, J. M. Scholey, and A. Mogilner. Early Spindle Assembly in Drosophila Embryos: Role of a Force Balance Involving Cytoskeletal Dynamics and Nuclear Mechanics. Molecular Biology of the Cell, 16(10):4967–4981, January 2005.

[137] Roy Wollman, Gul Civelekoglu-Scholey, Jonathan M Scholey, and Alex Mogilner. Reverse engineering of force integration during mitosis in the Drosophila embryo. Molecular Systems Biology, 4, May 2008.

[138] Gul Civelekoglu-Scholey and Jonathan M. Scholey. Mitotic force generators and chromosome segregation. Cellular and Molecular Life Sciences, 67(13):2231–2250, July 2010.

[139] Yuta Shimamoto, Scott Forth, and Tarun M. Kapoor. Measuring Pushing and Braking Forces Generated by Ensembles of Kinesin-5 Crosslinking Two Microtubules. Developmental Cell, 34(6):669–681, September 2015.

[140] Christian Hentrich and Thomas Surrey. Microtubule organization by the antagonistic mitotic motors kinesin-5 and kinesin-14. The Journal of Cell Biology, 189(3):465–480, March 2010.

[141] J. C. Waters, T. J. Mitchison, C. L. Rieder, and E. D. Salmon. The kinetochore microtubule minus-end disassembly associated with poleward flux produces a force that can do work. Molecular Biology of the Cell, 7(10):1547–1558, January 1996.

[142] R. Bruce Nicklas. How Cells Get the Right Chromosomes. Science, 275(5300):632–637, January 1997.

[143] Mark R. Flory, Mary Morphew, James D. Joseph, Anthony R. Means, and Trisha N. Davis. Pcp1p, an Spc110p-related calmodulin target at the centrosome of the fission yeast Schizosaccharomyces pombe. Cell Growth & Differentiation: The Molecular Biology Journal of the American Association for Cancer Research, 13(2):47–58, February 2002.

[144] Eric G. D. Muller, Brian E. Snydsman, Isabella Novik, Dale W. Hailey, Daniel R. Gestaut, Christine A. Niemann, Eileen T. O'Toole, Tom H. Giddings, Bryan A. Sundin, and Trisha N. Davis. The Organization of the Core Proteins of the Yeast Spindle Pole Body. Molecular Biology of the Cell, 16(7):3341–3352, January 2005.

[145] Marcel E. Janson, Mathilde E. de Dood, and Marileen Dogterom. Dynamic instability of microtubules is regulated by force. The Journal of Cell Biology, 161(6):1029–1034, June 2003.

[146] Marileen Dogterom and Bernard Yurke. Measurement of the Force-Velocity Relation for Growing Microtubules. Science, 278(5339):856–860, October 1997.

[147] Tim Mitchison and Marc Kirschner. Dynamic instability of microtubule growth. Nature, 312(5991):237–242, November 1984.

bioRxiv preprint doi: https://doi.org/10.1101/649913; this version posted October 22, 2019. The copyright holder for this preprint (which was not certified by peer review) is the author/funder. All rights reserved. No reuse allowed without permission.

[148] Yu-Guo Tao, W. K. den Otter, J. T. Padding, J. K. G. Dhont, and W. J. Briels. Brownian dynamics simulations of the self- and collective rotational diffusion coefficients of rigid long thin rods. The Journal of Chemical Physics, 122(24):244903–244903–10, June 2005.

[149] Ioana M. Ilie, Wim J. Briels, and Wouter K. den Otter. An elementary singularity-free Rotational Brownian Dynamics algorithm for anisotropic particles. The Journal of Chemical Physics, 142(11):114103, March 2015.

[150] Conrad Sanderson and Ryan Curtin. Armadillo: A template-based C++ library for linear algebra. https://joss.theoj.org, June 2016.

[151] Conrad Sanderson and Ryan Curtin. Practical Sparse Matrices in C++ with Hybrid Storage and Template-Based Expression Optimisation. Mathematical and Computational Applications, 24(3):70, September 2019.

[152] Imre Derényi, Frank Jülicher, and Jacques Prost. Formation and Interaction of Membrane Tubes. Physical Review Letters, 88(23):238101, May 2002.

[153] Gerald H. W. Lim, Greg Huber, Yoshihiro Torii, Aiko Hirata, Jonathan Miller, and Shelley Sazer. Vesicle-Like Biomechanics Governs Important Aspects of Nuclear Geometry in Fission Yeast. PLoS ONE, 2(9):e948, September 2007.

[154] Jared C. Cochran, Christopher A. Sontag, Zoltan Maliga, Tarun M. Kapoor, John J. Correia, and Susan P. Gilbert. Mechanistic Analysis of the Mitotic Kinesin Eg5. Journal of Biological Chemistry, 279(37):38861–38870, October 2004.

[155] Kenji Kawaguchi and Shin-ichi Ishiwata. Nucleotide-Dependent Single- to Double-Headed Binding of Kinesin. Science, 291(5504):667–669, January 2001.

[156] Johanna Roostalu, Christian Hentrich, Peter Bieling, Ivo A. Telley, Elmar Schiebel, and Thomas Surrey. Directional Switching of the Kinesin Cin8 Through Motor Coupling. Science, 332(6025):94–99, January 2011.

[157] Adina Gerson-Gurwitz, Christina Thiede, Natalia Movshovich, Vladimir Fridman, Maria Podolskaya, Tsafi Danieli, Stefan Lakämper, Dieter R. Klopfenstein, Christoph F. Schmidt, and Larisa Gheber. Directionality of individual kinesin-5 Cin8 motors is modulated by loop 8, ionic strength and microtubule geometry. The EMBO Journal, 30(24):4942, December 2011.

[158] A. S. Kashina, R. J. Baskin, D. G. Cole, K. P. Wedaman, W. M. Saxton, and J. M. Scholey. A bipolar kinesin. Nature, 379(6562):270–272, January 1996.

[159] Megan T. Valentine, Polly M. Fordyce, Troy C. Krzysiak, Susan P. Gilbert, and Steven M. Block. Individual dimers of the mitotic kinesin motor Eg5 step processively and support substantial loads in vitro. Nature Cell Biology, 8(5):470–476, May 2006.

[160] Göker Arpağ, Shankar Shastry, William O. Hancock, and Erkan Tüzel. Transport by Populations of Fast and Slow Kinesins Uncovers Novel Family-Dependent Motor Characteristics Important for In Vivo Function. Biophysical Journal, 107(8):1896–1904, October 2014.

bioRxiv preprint doi: https://doi.org/10.1101/649913; this version posted October 22, 2019. The copyright holder for this preprint (which was not certified by peer review) is the author/funder. All rights reserved. No reuse allowed without permission.

[161] Aurélien Bancaud, Sébastien Huet, Nathalie Daigle, Julien Mozziconacci, Joël Beaudouin, and Jan Ellenberg. Molecular crowding affects diffusion and binding of nuclear proteins in heterochromatin and reveals the fractal organization of chromatin. The EMBO Journal, 28(24):3785–3798, December 2009.

[162] Christina Thiede, Vladimir Fridman, Adina Gerson-Gurwitz, Larisa Gheber, and Christoph F. Schmidt. Regulation of bi-directional movement of single kinesin-5 Cin8 molecules. BioArchitecture, 2(2):70–74, March 2012.

[163] Vladimir Fridman, Adina Gerson-Gurwitz, Ofer Shapira, Natalia Movshovich, Stefan Lakämper, Christoph F. Schmidt, and Larisa Gheber. Kinesin-5 Kip1 is a bi-directional motor that stabilizes microtubules and tracks their plus-ends in vivo. J Cell Sci, 126(18):4147–4159, September 2013.

[164] Peter Bieling, Iva Kronja, and Thomas Surrey. Microtubule Motility on Reconstituted Meiotic Chromatin. Current Biology, 20(8):763–769, April 2010.

[165] Alison L. Pidoux and Robin C. Allshire. Kinetochore and heterochromatin domains of the fission yeast centromere. Chromosome Research, 12(6):521–534, September 2004.

[166] X. Liu, I. McLeod, S. Anderson, J. R. Yates, and X. He. Molecular analysis of kinetochore architecture in fission yeast. The EMBO Journal, 24(16):2919–2930, 2005.

[167] Isabel Sanchez-Perez, Steven J. Renwick, Karen Crawley, Inga Karig, Vicky Buck, John C. Meadows, Alejandro Franco-Sanchez, Ursula Fleig, Takashi Toda, and Jonathan B. A. Millar. The DASH complex and Klp5/Klp6 kinesin coordinate bipolar chromosome attachment in fission yeast. The EMBO Journal, 24(16):2931–2943, August 2005.

[168] Helder Maiato, Jennifer DeLuca, E. D. Salmon, and William C. Earnshaw. The dynamic kinetochore-microtubule interface. Journal of Cell Science, 117(23):5461–5477, November 2004.

[169] Iain M. Cheeseman, Joshua S. Chappie, Elizabeth M. Wilson-Kubalek, and Arshad Desai. The Conserved KMN Network Constitutes the Core Microtubule-Binding Site of the Kinetochore. Cell, 127(5):983–997, December 2006.

[170] Emily A. Foley and Tarun M. Kapoor. Microtubule attachment and spindle assembly checkpoint signalling at the kinetochore. Nature Reviews Molecular Cell Biology, 14(1):25, January 2013.

[171] Karthik Dhatchinamoorthy, Manjunatha Shivaraju, Jeffrey J. Lange, Boris Rubinstein, Jay R. Unruh, Brian D. Slaughter, and Jennifer L. Gerton. Structural plasticity of the living kinetochore. J Cell Biol, 216(11):3551–3570, November 2017.

[172] Donald L. Koch and Ganesh Subramanian. Collective Hydrodynamics of Swimming Microorganisms: Living Fluids. Annual Review of Fluid Mechanics, 43(1):637–659, 2011.

[173] Michael A. Lampson and Iain M. Cheeseman. Sensing centromere tension: Aurora B and the regulation of kinetochore function. Trends in Cell Biology, 21(3):133–140, March 2011.

bioRxiv preprint doi: https://doi.org/10.1101/649913; this version posted October 22, 2019. The copyright holder for this preprint (which was not certified by peer review) is the author/funder. All rights reserved. No reuse allowed without permission.

[174] Xue-song Liu, Xu-dong Zhao, Xiaoxing Wang, Yi-xin Yao, Liang-liang Zhang, Run-zhe Shu, Wei-hua Ren, Ying Huang, Lei Huang, Ming-min Gu, Ying Kuang, Long Wang, Shun-yuan Lu, Jun Chi, Jing-sheng Fen, Yi-fei Wang, Jian Fei, Wei Dai, and Zhu-Gang Wang. Germinal Cell Aplasia in Kif18a Mutant Male Mice Due to Impaired Chromosome Congression and Dysregulated BubR1 and CENP-E. Genes & Cancer, 1(1):26–39, January 2010.

[175] Michael P. Allen and Guido Germano. Expressions for forces and torques in molecular simulations using rigid bodies. Molecular Physics, 104(20-21):3225–3235, October 2006.

[176] Claudio Ciferri, Andrea Musacchio, and Arsen Petrovic. The Ndc80 complex: Hub of kinetochore activity. FEBS Letters, 581(15):2862–2869, June 2007.

[177] Charles L. Asbury, Daniel R. Gestaut, Andrew F. Powers, Andrew D. Franck, and Trisha N. Davis. The Dam1 kinetochore complex harnesses microtubule dynamics to produce force and movement. Proceedings of the National Academy of Sciences, 103(26):9873–9878, June 2006.

[178] Kenneth W Wood, Roman Sakowicz, Lawrence S. B Goldstein, and Don W Cleveland. CENP-E Is a Plus End–Directed Kinetochore Motor Required for Metaphase Chromosome Alignment. Cell, 91(3):357–366, October 1997.

[179] Imène B. Bouhlel, Midori Ohta, Adeline Mayeux, Nicole Bordes, Florent Dingli, Jérôme Boulanger, Guilhem Velve Casquillas, Damarys Loew, Phong T. Tran, Masamitsu Sato, and Anne Paoletti. Cell cycle control of spindle pole body duplication and splitting by Sfi1 and Cdc31 in fission yeast. J Cell Sci, 128(8):1481–1493, April 2015.

[180] I.-Ju Lee, Ning Wang, Wen Hu, Kersey Schott, Jürg Bähler, Thomas H. Giddings, John R. Pringle, Li-Lin Du, and Jian-Qiu Wu. Regulation of spindle pole body assembly and cytokinesis by the centrin-binding protein Sfi1 in fission yeast. Molecular Biology of the Cell, 25(18):2735–2749, September 2014.

[181] J. Kennedy and R. Eberhart. Particle swarm optimization. In Proceedings of the IEEE International Conference on Neural Networks, 1995, volume 4, pages 1942–1948 vol.4, November 1995.

Supplementary videos

Video S1

Simulation of reference model shows spindle assembly simultaneous with chromosome biorientation. Initially short MTs begin to grow at the start of the simulation and interact with nearby kinetochores. A bipolar spindle forms as the chromosomes begin to biorient. Finally, a metaphase spindle is established with bioriented chromosomes that move along the spindle and breathe. The insets are zoomed views of each chromosome, showing attachment turnover and interkinetochore stretch.

bioRxiv preprint doi: https://doi.org/10.1101/649913; this version posted October 22, 2019. The copyright holder for this preprint (which was not certified by peer review) is the author/funder. All rights reserved. No reuse allowed without permission.

Video S2

Top: Simulation of reference model (left) and simulated fluorescence microscopy images (right), with red MTs and green kinetochore (scale bar 1 μm). The simulated fluorescence images are rotated so that the spindle is vertical. Lower: simulation of models mimicking genetic perturbation. Lower left: Model lacking kinesin-5 motors. The SPBs never separate and the spindle remains monopolar. Chromosomes do not biorient. Lower right: Model lacking crosslinker-mediated stabilization of MT dynamics. SPBs separate only slightly, forming a short spindle that is nearly indistinguishable from a monopolar spindle. Chromosomes do not biorient.

Video S3

Simulation of a model with a soft nuclear envelope and an asymptotic wall force on the SPBs of 17 pN. SPBs are able to move away from their preferred radius from the center of the nucleus. The spindle reaches a bounded length, and chromosomes are able to biorient. Spindle length larger than the nuclear envelope radius are reached by the balance of the nuclear envelope force and the forces from motors, crosslinkers, and chromosomes.

Video S4

Simulations of models with perturbation to kinetochore properties important for biorientation. Top left: Model lacking progressive restriction, with a common angular spring stiffnesses of 1 $\mathrm{k_B T}$ for all attachments. A short bipolar spindle forms, but chromosomes are typically merotelically attached and do not biorient. Top middle: Model lacking progressive restriction, with a common angular spring stiffnesses of 100 $\mathrm{k_B T}$ for all attachments. A long bipolar spindle forms, kinetochore-MT attachments are transient, and chromosomes do not generate significant inward force on the spindle. Top right: Model including progressive restriction with an angular spring stiffness of 20 $\mathrm{k_B T}$ for the first binding event, leading to restricted attachments. A long bipolar spindle forms, and kinetochore-MT attachments are transient. Lower left: model including progressive restriction but with an angular spring stiffness of 20 $\mathrm{k_B T}$ for the third binding event, leading to permissive attachments. Error correction is impaired, and chromosomes are typically merotelically attached. Lower middle: Model lacking misaligned destabilization. Error correction is impaired. Lower right: Model with force-independent attachment kinetics. Kinetochore-MT attachments are not stabilized under tension from depolymerizing microtubules, leading to short-lived biorientation.

Video S5

Simulation of a model with interkinetochore force-dependent attachments. The interkinetochore characteristic force is set at 1.67 pN for this model. The spindle forms in a few minutes, and chromosomes form stable, bioriented attachments. Zoomed views of chromosomes shows them forming load-bearing attachments to the tips of MTs.

bioRxiv preprint doi: https://doi.org/10.1101/649913; this version posted October 22, 2019. The copyright holder for this preprint (which was not certified by peer review) is the author/funder. All rights reserved. No reuse allowed without permission.

Video S6

Simulations of models with varying kinetochore-MT attachment lifetime. Left: Model with short attachment lifetime in which the kinetochore-MT binding and unbinding rates are 4 times larger than in the reference model. Biorientation is somewhat compromised. Middle: Model with intermediate attachment lifetime in which the kinetochore-MT binding and unbinding rates are 2 times larger than in the reference model. Right: Model with long attachment lifetime in which the kinetochore-MT binding and unbinding rates are 2 times smaller than in the reference model. Biorientation is preserved and the spindle undergoes large length fluctuations.

Video S7

Simulations of reference, restricted, and weak rescue models. Left: The reference model shows typical spindle length fluctuations. Middle: The restricted attachment model shows minimal length fluctuations, because transient kinetochore-MT attachments lead to low inward force on the spindle from chromosomes. Right: The weak rescue model shows large spindle length fluctuations, because kinetochore MTs remain attached while depolymerizing, leading to high and fluctuating inward force on the spindle from chromosomes.

Video S8

Simulations of anaphase chromosome segregation. Anaphase occurs at 7:09. Top: Simulation video showing that separation of the sister chromatids occurs after 4.45 minutes of the simultaneous biorientation of all three chromosomes. The zoomed views show the chromosomes achieving this biorientation, before segregating to the spindle poles. Lower: Simulation video (left) and simulated fluorescence microscopy images (right), with red MTs and green kinetochore (scale bar 1 μm). The simulated fluorescence images are rotated so that the spindle is vertical.

A Appendix: extended methods

A.1 Computational model

Our group has developed a simulation framework for microtubule-motor active matter and mitotic spindle self-assembly [52, 62, 63, 65, 66]. The computational scheme alternates between Brownian dynamics (BD) and kinetic Monte Carlo (kMC) steps to evolve the system forward in time. BD describes how particles move in response to forces and torques in a highly viscous medium. KMC methods handle stochastic state transitions, such as binding and dynamic instability [63].

A.1.1 Microtubules (MTs)

MTs are built of α- and β-tubulin subunits that join end-to-end to form protofilaments. $\sim$13 side-by-side protofilaments form a hollow cylinder with distinct plus- and minus-ends. MTs undergo dynamic instability, in which they grow and shrink with speeds v_g and v_s, transition from a shrinking state to a growing state (rescue) at rate f_r, and transition from growing to shrinking (catastrophe) at rate f_c [147]. MT catastrophe rate increases with compressive force [145].

bioRxiv preprint doi: https://doi.org/10.1101/649913; this version posted October 22, 2019. The copyright holder for this preprint (which was not certified by peer review) is the author/funder. All rights reserved. No reuse allowed without permission.

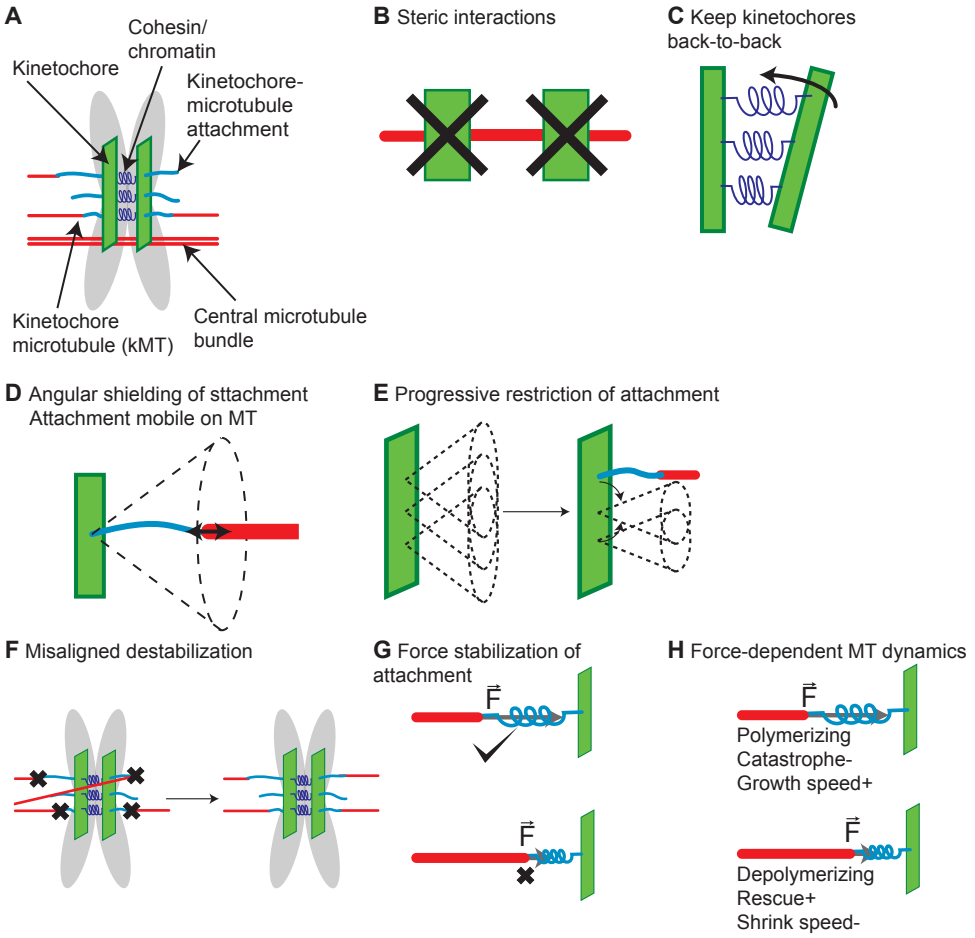

Figure 9: **Chromosome model overview (A)** Chromosomes are modeled as sister chromatids and kinetochores held together by a cohesin/chromatin spring complex. Each kinetochore can attach up to three microtubules. **(B)** Steric interactions between MTs and kinetochores prevent overlap, while a soft steric repulsion exists between MTs and the centromeric DNA. **(C)** Kinetochores are kept back-to-back through a cohesin-chromatin spring complex that depends on relative kinetochore position and orientation. **(D)** The angular range of kinetochore-MT attachment is restricted based on the stiffness of an angular spring. **(E)** The angular restriction of kinetochore-MT attachment changes based on the number of bound MTs. **(F)** Attachments are destabilized when the chromosome is not properly bioriented. **(G)** Attachment lifetime is force-dependent, with attachments to depolymerizing MTs under tension having longer lifetimes, while those to polymerizing MTs have their lifetime decreased under tension. **(H)** MT dynamics are force-dependent. Polymerizing MTs have increased growth speed and reduced catastrophe, while depolymerizing MTs have increased rescue and decreased shrinking speed.

We model MTs as growing and shrinking spherocylinders that experience steric repulsion with other MTs and molecules. The typical MT length in fission yeast spindles ($\sim 1\mu$m) is much shorter than the MT persistence length ($\sim$ 1mm), so we treat MTs inflexible filaments [148]. Each MT has a center-of-mass coordinate $\mathbf{x}$, orientation $\mathbf{u}$, and length L [63]. The MT position evolves according to

$$\mathbf{x}_i(t+\delta t) = \mathbf{x}_i(t) + \mathbf{\Gamma}_i^{-1}(t) \cdot \mathbf{F}_i(t)\delta t + \delta\mathbf{x}_i(t), \tag{1}$$

bioRxiv preprint doi: https://doi.org/10.1101/649913; this version posted October 22, 2019. The copyright holder for this preprint (which was not certified by peer review) is the author/funder. All rights reserved. No reuse allowed without permission.

Simulation parameter	**Symbol**	**Value**	**Notes**
Time step	δt	8.9×10^{-6} s	[63]
Nuclear envelope radius	R	1.375 μm	[77]
Spindle pole bodies			
Diameter	σ_{SPB}	0.1625 μm	[98]
Bridge size		75 nm	[98]
Tether rest length	R_0	50 nm	[143, 144]
Tether spring constant	K_0	0.6625 pN nm^{-1}	[63]
Translational diffusion coefficient	D_t	4.5×10^{-4} μm^2 s^{-1}	[63]
Rotational diffusion coefficient	$D_{\theta,\mathrm{spb}}$	0.0170 s^{-1}	[63]
Linkage time	τ_{link}	5 s	[63]
Microtubules			
Diameter	σ_{MT}	25 nm	[63]
Angular diffusion coefficient	D_θ	Depends on MT length	[63, 77]
Force-induced catastrophe constant	α_c	0.5 pN^{-1}	[63, 145, 146]
Growth speed	$v_{p,0}$	4.1 μm min^{-1}	[62, 63]
Shrinking speed	$v_{s,0}$	6.7 μm min^{-1}	[62, 63]
Catastrophe frequency	$f_{c,0}$	3.994 min^{-1}	[62, 63]
Rescue frequency	$f_{r,0}$	0.157 min^{-1}	[62, 63]
Growth speed stabilization	s_{vg}	1.54	Optimized
Shrinking speed stabilization	s_{vs}	0.094	Optimized
Catastrophe frequency stabilization	s_{fc}	0.098	Optimized
Rescue frequency stabilization	s_{fr}	18	Optimized
Stabilization length	s_ℓ	16 nm	Optimized
Minimum MT length	$L_{\min}$	75 nm	

Table 1: Simulation, SPB, and MT parameters.

where the random displacement $\delta\mathbf{x}_i(t)$ is Gaussian-distributed and anisotropic, with variance

$$\langle \delta\mathbf{x}_i(t)\delta\mathbf{x}_i(t)\rangle = 2k_BT\mathbf{\Gamma}_i^{-1}(t)\delta t, \tag{2}$$

and $\mathbf{\Gamma}_i^{-1}(t)$ is the inverse friction tensor

$$\mathbf{\Gamma}_i^{-1}(t) = \gamma_{\parallel}^{-1}\mathbf{u}_i(t)\mathbf{u}_i(t) + \gamma_{\perp}^{-1}\left[\mathbf{I} - \mathbf{u}_i(t)\mathbf{u}_i(t)\right], \tag{3}$$

where $\gamma_{\parallel}$ and $\gamma_{\perp}$ are the parallel and perpendicular drag coefficients, and $\mathbf{F}_i(t)$ is the force on filament i at time t. MT orientation evolves according to

$$\mathbf{u}_i(t+\delta t) = \mathbf{u}_i(t) + \frac{1}{\gamma_r}\mathbf{T}_i(t) \times \mathbf{u}_i(t)\delta t + \delta\mathbf{u}_i(t), \tag{4}$$

where γ_r is the rotational drag coefficient, $\mathbf{T}_i(t)$ the torque, and $\delta\mathbf{u}_i(t)$ the random reorientation, which is Gaussian distributed with variance

$$\langle \delta\mathbf{u}_i(t)\delta\mathbf{u}_i(t)\rangle = 2k_BT/\gamma_r\left[\mathbf{I} - \mathbf{u}_i(t)\mathbf{u}_i(t)\right]\delta t, \tag{5}$$

bioRxiv preprint doi: https://doi.org/10.1101/649913; this version posted October 22, 2019. The copyright holder for this preprint (which was not certified by peer review) is the author/funder. All rights reserved. No reuse allowed without permission.

where $\mathbf{I}$ is the identity matrix.

The drag coefficients $\gamma_{\parallel}$, $\gamma_{\perp}$, and γ_r are recalculated at each time step based on the MT length L [62,63,83–85]. Random translation and reorientation are treated in the body-frame of the MT. Random parallel displacements are

$$\delta x_{\parallel} = s_{\text{random}} \sqrt{\frac{2k_B T \delta t}{\gamma_{\parallel}}} R(t), \tag{6}$$

where $R(t)$ is a Gaussian random variate with $\sigma = 1.0$, and s_{random} varies the strength of the random forces if necessary. Perpendicular displacements are

$$\delta x_{\perp} = s_{\text{random}} \sqrt{\frac{2k_B T \delta t}{\gamma_{\perp}}} R(t), \tag{7}$$

for each perpendicular dimension of the MT in the body-frame. Random reorientations are

$$\delta u = s_{\text{random}} \sqrt{\frac{2k_B T \delta t}{\gamma_r}} R(t), \tag{8}$$

for each angle of the MT in the body-frame.

We model dynamic instability as a continuous stochastic process in which MTs in the polymerizing state grow with speed v_g, while those in the shrinking state depolymerize with speed v_s. MTs undergo catastrophe at rate $f_{c,0}$ and rescue at rate $f_{r,0}$. These rates are modified by interactions with crosslinkers, kinetochores, and the nuclear envelope. At each time step, kinetic Monte Carlo sampling is used to determine dynamic state transitions. Each MT stochastically switches between its states according to the dynamic instability parameters (Table 1) [63, 77]. Using previous methods [62, 63, 145, 146], force-induced catastrophe is implemented at MT plus-ends, according to an exponential force term $f_{\text{cat}}(\mathbf{F}_{\parallel}) = f_{\text{cat},0} e^{\alpha_c \mathbf{F}_{\parallel}}$. Rather than explicitly modeling MT nucleation, we have chosen to have a fixed number of MTs with maximum and minimum length. When MTs reach the minimum length while undergoing catastrophe, they switch to the growing state. However, MTs that reach their maximum length pause, ensuring numerical stability for barrier interactions.

We model steric repulsion using the Weeks-Chandler-Anderson (WCA) potential

$$u_{\text{wca}}(r_{\min}) = \begin{cases} 4k_B T \left[\left(\frac{\sigma_{\text{MT}}}{r_{\min}} \right)^{12} - \left(\frac{\sigma_{\text{MT}}}{r_{\min}} \right)^{6} \right] + k_B T, & r_{\min} < 2^{1/6} \sigma_{\text{MT}} \\ 0, & r_{\min} \geq 2^{1/6} \sigma_{\text{MT}}, \end{cases} \tag{9}$$

where $r_{\min}$ is the minimum distance between two finite line segments of length l that defines the filament axes and σ_{MT} the effective rod diameter. Large forces are capped at a fixed value based on the size of the time step to prevent numerical instability [83].

A.1.2 Nuclear envelope

The nuclear envelope is modeled as a shell of fixed radius R centered at the origin. As for MT-MT interactions, MT-nuclear envelope interactions use the WCA potential

$$u_{\text{wca,MT}}(r_{\min}) = \begin{cases} 4k_B T \left[\left(\frac{\sigma_{MT}}{r_{\min}} \right)^{12} - \left(\frac{\sigma_{MT}}{r_{\min}} \right)^{6} \right] + k_B T, & r_{\min} < 2^{1/6} \sigma_{MT} \\ 0, & r_{\min} \geq 2^{1/6} \sigma_{MT}, \end{cases} \tag{10}$$

bioRxiv preprint doi: https://doi.org/10.1101/649913; this version posted October 22, 2019. The copyright holder for this preprint (which was not certified by peer review) is the author/funder. All rights reserved. No reuse allowed without permission.

where $r_{\min}$ is the minimum distance between the free end of the MT and the enclosing sphere with radius $R + \sigma_{MT}/2$. This allows for smooth continuation of the dynamics at the nuclear envelope, which has an effective radius of R. Similar to the MT-MT interactions, forces are capped to prevent instabilities for rare high-overlap events. As mentioned previously, the MT-nuclear envelope interaction enhances MT catastrophe (Table 1).

A.1.3 Spindle pole bodies

Spindle pole bodies (SPBs), the centrosomes of fission yeast, are embedded in the nuclear envelope during mitosis. MT minus-ends are tethered to the SPBs. We model SPBs as spherical caps confined to the surface of the nuclear envelope [63]. Each SPB has a right-handed coordinate system defined by $\hat{\mathbf{u}}$ which points inward from the SPB, and $\hat{\mathbf{v}}$ and $\hat{\mathbf{w}}$ which are arbitrary and perpendicular to one another. The equations of motion for an SPB constrained to move on the surface of the nuclear envelope are

$$\mathbf{u}_i(t+\delta t) = \mathbf{u}_i(t) - \frac{1}{R\gamma_t}\mathbf{F}_{||}(t)\delta t + \delta\mathbf{u}_i(t), \tag{11}$$

where $\mathbf{F}_{||}$ is the force in the plane tangent to the SPB and $\delta\mathbf{u}_i(t)$ is Gaussian-distributed with variance $\langle\delta\mathbf{u}_i(t)\delta\mathbf{u}_i(t)\rangle = \frac{2\mathrm{k_B T}}{R^2\gamma_t}(\mathbf{I} - \mathbf{u}_i(t)\mathbf{u}_i(t))\delta t$. The corresponding rotational equation of motion for an SPB about its center is

$$\mathbf{v}_i(t+\delta t) = \mathbf{v}_i(t) + \frac{1}{\gamma_r}\mathbf{T}_{i,\mathrm{body}}(t) \times \mathbf{v}_i(t)\delta t + \delta\mathbf{v}_i(t), \tag{12}$$

where $\mathbf{T}_{i,\mathrm{body}}$ is the torque on the SPB about the axis defined by $\mathbf{u}_i$.

The SPBs repel each other via the WCA potential

$$u_{\mathrm{wca,SPB}}(\delta r_{\mathrm{eff}}) = \begin{cases} 4k_BT\left[\left(\frac{\sigma_{\mathrm{MT}}}{\delta r_{\mathrm{eff}}}\right)^{12} - \left(\frac{\sigma_{\mathrm{MT}}}{\delta r_{\mathrm{eff}}}\right)^{6}\right] + k_BT, & \delta r_{\mathrm{eff}} < 2^{1/6}\sigma_{\mathrm{MT}} \\ 0, & \delta r_{\mathrm{eff}} \geq 2^{1/6}\sigma_{\mathrm{MT}}, \end{cases} \tag{13}$$

where $\delta r_{\mathrm{eff}} = \delta r - \sigma_{\mathrm{SPB}} + \sigma_{\mathrm{MT}}$.

Each SPB tethers the minus-ends of 14 MTs. Since the SPBs are three-dimensional rigid bodies confined to move on a two-dimensional surface, they have a fixed right-handed coordinate system that transforms according to the translation and rotation of the SPB. The attachment sites of the MT minus-ends are specified using this coordinate system. The tethers are modeled by a harmonic potential

$$u_{\mathrm{teth}}(\mathbf{r}_{\mathrm{MT,i}}, \mathbf{r}_{\mathrm{teth,i}}) = \frac{1}{2}K_0\left(\left|\mathbf{r}_{\mathrm{MT,i}} - \frac{L_i}{2}\hat{\mathbf{u}}_{\mathrm{MT,i}} - \mathbf{r}_{\mathrm{teth,i}}\right| - R_0\right)^2, \tag{14}$$

where L_i is the length of MT i, $\mathbf{r}_{\mathrm{MT,i}}$ and $\hat{\mathbf{u}}_{\mathrm{MT,i}}$ are the center of mass position and unit orientation vector for MT i respectively, and $\mathbf{r}_{\mathrm{teth,i}}$ is the vector connecting MT i's tether position on the spindle pole body to the minus end of MT i. Torques on the MT are calculated using the force applied to the minus end of the MT associated with tether i. The tether springs do not interact with one another or any other objects in the system other than through the tethering potential (Table 1).

bioRxiv preprint doi: https://doi.org/10.1101/649913; this version posted October 22, 2019. The copyright holder for this preprint (which was not certified by peer review) is the author/funder. All rights reserved. No reuse allowed without permission.

A.1.4 Soft nuclear envelope

In our model, SPBs are confined to move on a spherical shell of radius R, and MTs experienced a steric interaction with this spherical shell. This limits the physical realism of the model, because it neglects the ability of the nuclear envelope to deform under force. The rigid nuclear envelope could lead to situations where the force on the spindle from the nuclear envelope sets the spindle length, rather than allowing spindle length to be determined by force balance between the nuclear envelope, motor and crosslinker proteins, and chromosomes. In order to address this issue, we have implemented changes to more realistically model the interactions between MTs, SPBs, and the nuclear envelope.

In the soft nuclear envelope model, SPBs are no longer confined to move on the spherical shell of the nuclear envelope. Instead, SPBs can freely translate and rotate in three dimensions. For the SPBs we implemented previously developed algorithms for 3D translational and rotational movement of rigid Brownian objects [149]. In this model, each SPB is defined by its center of mass coordinates $\mathbf{r}_i(t)$ and a quaternion describing its orientation $\mathbf{q}_i(t)$. This quaternion allows for the exact description of the unit coordinate axes that lie on the surface of the SPB ($\mathbf{u}$, $\mathbf{v}$, and $\mathbf{w}$). Translational motion for each SPB is described by the equation

$$r_\alpha(t+\Delta t) - r_\alpha(t) = A_{\alpha\gamma}\mu^{tb}_{\gamma\delta}A_{\beta\delta}F_\beta\Delta t + A_{\alpha\gamma}(\sqrt{\mu^{tb}})_{\gamma\beta}\Theta^t_\beta\sqrt{2k_BT\Delta t}, \tag{15}$$

where $\mathbf{A}$ is the current rotation matrix describing the orientation of the SPB expressed in its homogeneous form, μ^{tb} is the translation mobility matrix, $\mathbf{F}$ is the applied force, and $\mathbf{\Theta}$ is a vector of three uncorrelated gaussian numbers with zero mean and unit variance. The rotational motion of each SPB is described by the change in its orientation quaternion

$$q_a(t+\Delta t) - q_a(t) = B_{a\alpha}\mu^{rb}_{\gamma\delta}A_{\gamma\beta}T^s_\gamma\Delta t + B_{a\alpha}(\sqrt{\mu^{rb}})_{\alpha\beta}\Theta^q_\beta\sqrt{wk_BT\Delta t} + \lambda_q q_\alpha, \tag{16}$$

where $\mathbf{B}$ is a matrix described by the elements of the quaternion

$$\mathbf{B} = \frac{1}{2q^4}\begin{pmatrix} q_0 & -q_1 & -q_2 & -q_3 \\ q_1 & q_0 & -q_3 & q_2 \\ q_2 & q_3 & q_0 & -q_1 \\ q_3 & -q_2 & q_1 & q_0 \end{pmatrix}, \tag{17}$$

and $\mathbf{T}^s$ is the torque in the lab coordinate frame on the SPB, $\mathbf{\Theta}$ is a vector of three uncorrelated gaussian numbers with zero mean and unit variance, and λ_q is a Lagrange multiplier satisfying the condition

$$\lambda_q^2 + 2\lambda_q\mathbf{q}(t)\cdot\tilde{\mathbf{q}}(t+\Delta t) + \tilde{\mathbf{q}}^2(t+\Delta t) = 1, \tag{18}$$

where $\tilde{\mathbf{q}}(t+\Delta t)$ is the quaternion after an unconstrained time step in Δt [149]. We implemented these equations using the Armadillo C++ framework for linear algebra [150, 151].

In previous work the interaction between MTs and a deformable nuclear envelope [65, 66]. Here, we use this same force model to describe the interactions between MT plus-ends and the nuclear envelope, and a similar force between SPBs and the nuclear envelope. This force takes on the form in the linear regime of

$$F_{lin}(L) = \frac{F_w}{R_{tube}(ln(2)-\gamma)}L \tag{19}$$

where L is the distance the SPB (or MT) protrudes from the wall, and F_w is the asymptotic wall force, γ is Euler's constant, and R_{tube} is the characteristic membrane tube radius. The non-monotonic regime is

bioRxiv preprint doi: https://doi.org/10.1101/649913; this version posted October 22, 2019. The copyright holder for this preprint (which was not certified by peer review) is the author/funder. All rights reserved. No reuse allowed without permission.

Parameter	Symbol	Value	Notes
Translation mobility	μ^{tb}_{SPB}	$\begin{pmatrix} 0.05 & 0 & 0 \\ 0 & 0.11 & 0 \\ 0 & 0 & 0.11 \end{pmatrix}$ μm s^{-1} pN-1	Calculated
Rotation mobility	μ^{rb}_{SPB}	$\begin{pmatrix} 16.6 & 0 & 0 \\ 0 & 0.166 & 0 \\ 0 & 0 & 0.166 \end{pmatrix}$ μm^{-1} s^{-1} pN^{-1}	Calculated
Membrane tube radius	f_{tube}	87.7 nm	[65, 152, 153]
MT asymptotic wall force	$f_{\mathrm{MT,w}}$	2.5 pN	[65, 152, 153]
SPB asymptotic wall force	$f_{\mathrm{SPB,w}}$	17 pN	[65, 152, 153]
Tether spring constant	K_0	6.625 pN nm^{-1}	Optimized

Table 2: Soft nuclear envelope model parameters.

governed by the equation

$$F_{asymp}(L) = 2aF_w e^{\frac{-L}{b}} cos(\frac{L}{b} + c) + F_w \tag{20}$$

where a = 0.5416... is an integration constant, b is $\sqrt{2R_{tube}}$, and c = 4.038... These two equations can be added together, multiplying the non-monotonic equation by a factor of $(1 - e^{-L})$ to correct the boundary condition at $L = 0$ [65,66]. For SPBs, this force is exerted when they are moved away from the preferred radius of the NE R, and only in the radial direction. In addition, we implemented a reorientation torque that causes the SPBs to prefer pointing into the nucleus of the form

$$\mathbf{T}_{\mathrm{SPB,NE,i}} = -\kappa_{\mathrm{r,SPB,NE}}(\hat{\mathbf{u}}_i \cdot \hat{\mathbf{r}}_i + 1)(\hat{\mathbf{u}}_i \times \hat{\mathbf{r}}_i) \tag{21}$$

where $\kappa_{\mathrm{SPB,NE}}$ is the angular spring constant of this interaction. MT minus-ends no longer interact with the nuclear envelope, instead only interacting through their tethers to SPBs.

The soft nuclear envelope model requires the translation and rotation mobility matrices describing the motion of SPBs ($\mu_{\mathrm{SPB,tb}}$ and $\mu_{\mathrm{SPB,rb}}$). These are based on the diffusion of SPBs (Table 1). The wall force is described by a membrane tube radius f_{tube} and asymptotic wall force for both MTs $f_{\mathrm{MT,w}}$ and SPBs $f_{\mathrm{SPB,w}}$ [65]. SPB-MT tether spring constants were increased to stiffen the interaction between MT minus-ends and the SPBs.

A.1.5 Motors and crosslinkers

We model kinesin-5 motors (Cut7), kinesin-14 motors (Pkl1 and Klp2), and crosslinkers (Ase1). Kinesin-5 motors in the model are plus-end directed only when crosslinking antiparallel MTs; otherwise, they are minus-end directed [63,86,89,156,157,162,163]. Kinesin-14 motors are minus-end directed [13–15,90–93]. Crosslinkers have an increased binding affinity for antiparallel MTs [17, 19, 20, 95]. Motors move directionally with a force-dependent velocity based on their stall force, and both motor and crosslinker heads diffuse along MTs while bound (Table 3).

The number of active motors and crosslinkers in the model is constrained by experimental data, which estimated total molecule numbers by mass spectrometry and found that mitotic fission-yeast cells have on average 1610 Cut7 tetramers, 2440 Pkl1 and Klp2 dimers (combined), and 3613 Klp9 tetramers and Ase1 dimers (combined) [118]. We considered these numbers as upper bounds, because of the molecules present in the cell, many may not be active in the spindle because they are outside the nucleus, inactive, and/or in the process of being produced or degraded. We therefore allowed the number of active molecules to vary with the experimental values as an upper bound.

bioRxiv preprint doi: https://doi.org/10.1101/649913; this version posted October 22, 2019. The copyright holder for this preprint (which was not certified by peer review) is the author/funder. All rights reserved. No reuse allowed without permission.

Kinesin-5	**Symbol**	**Value**	**Notes**
Number	N_{K5}	174	Optimized, [118]
Association constant per site	K_a	90.9 μM^{-1} site^{-1}	[154]
One-dimensional effective concentration	c_2	0.4 nm^{-1}	[63]
Spring constant	K	0.3 pN nm^{-1}	[155]
Singly-bound velocity	v_0	-100 nm s^{-1}	[156]
Polar aligned velocity	$v_{0,P}$	-50 nm s^{-1}	[157]
Anti-polar aligned velocity	$v_{0,AP}$	8 nm s^{-1}	[157]
Singly bound off-rate	k_1	0.11 s^{-1}	[156]
Doubly bound off-rate (single head)	k_2	0.055 s^{-1}	[63]
Rest length	R_0	53 nm	[158]
Stall force	F_s	5 pN	[159]
Characteristic distance	x_c	1.5 nm	Optimized, [160]
Diffusion constant (solution)	D_{free}	4.5 μm^2 s^{-1}	[161]
Kinesin-14			
Number	N_{K14}	230	Optimized, [118]
Association constant (motor head)	$K_{a,m}$	22.727 μM^{-1} site^{-1}	[14]
Association constant (passive head)	$K_{a,d}$	22.727 μM^{-1} site^{-1}	[63]
1D effective concentration (motor head)	c_{2m}	0.1 nm^{-1}	[63]
1D effective concentration (passive head)	c_{2d}	0.1 nm^{-1}	[63]
Spring constant	K	0.3 pN nm^{-1}	[155]
Singly bound velocity (motor head)	v_{0m}	-50 nm s^{-1}	[63]
Diffusion constant (bound, diffusing head)	D_d	0.1 μm^2 s^{-1}	[63]
Singly bound off-rate (motor head)	k_{1m}	0.11 s^{-1}	[63]
Singly bound off-rate (passive head)	k_{1d}	0.1 s^{-1}	[63]
Doubly bound off-rate (motor head)	k_{2m}	0.055 s^{-1}	[63]
Doubly bound off-rate (passive head)	k_{2d}	0.05 s^{-1}	[63]
Rest length	R_0	53 nm	[63]
Stall force	F_s	5.0 pN	[63]
Characteristic distance	x_c	4.8 nm	Optimized, [160]
Crosslinker			
Number	N_{XL}	657	Optimized, [118]
Association constant	K_a	90.9 μM^{-1} site^{-1}	[154]
One-dimensional effective concentration	c_2	0.4 nm^{-1}	[20]
Spring constant	K	0.207 pN nm^{-1}	[20]
Diffusion constant (solution)	D_{free}	4.5 μm^2 s^{-1}	[161]
Singly bound diffusion constant	D_{sb}	$0.1 \times \mu$m^2 s^{-1}	[20]
Doubly bound diffusion constant	D_{db}	$0.0066667 \times \mu$m^2 s^{-1}	[20]
Singly bound off-rate	k_1	0.1 s^{-1}	[95]
Doubly bound off-rate	k_2	0.05 s^{-1}	[20]
Parallel-to-antiparallel bindng ratio	P_{aff}	0.33	[65, 66, 95]
Characteristic distance	x_c	2.1 nm	Optimized, [160]
Rest length	53 nm	[20, 65]	

Table 3: Motor and crosslinker parameters

bioRxiv preprint doi: https://doi.org/10.1101/649913; this version posted October 22, 2019. The copyright holder for this preprint (which was not certified by peer review) is the author/funder. All rights reserved. No reuse allowed without permission.

Motors and crosslinkers exert forces and torques on MTs when two heads are bound to two different MTs. The harmonic potential for doubly-bound motors and crosslinkers is

$$u_m(\mathbf{r}_{\mathrm{MT,i}}, \mathbf{r}_{\mathrm{MT,j}}) = \frac{1}{2}K_{m,0}\left(\left|\mathbf{r}_{\mathrm{MT,j}} + \left(s_j - \frac{L_j}{2}\right)\hat{\mathbf{u}}_{\mathrm{MT,j}} - \mathbf{r}_{\mathrm{MT,i}} - \left(s_i - \frac{L_i}{2}\right)\hat{\mathbf{u}}_{\mathrm{MT,i}}\right| - R_{m,0}\right)^2, \tag{22}$$

where s_i and s_j denote the motor/crosslinker head location on MTs i and j, L_i and L_j denote the MT lengths, and $R_{m,0}$ is the rest length of the spring. This potential determines the rate of binding/unbinding of crosslinkers in the singly-bound to doubly-bound state. The motors and crosslinkers do not interact with one another.

MT dynamic instability is altered by doubly bound crosslinkers [53, 164]. We change the dynamic instability parameters when a motor or crosslinker is within the threshold distance s_l of the plus-end of the MT according to

$$\begin{aligned} f_c &= f_{c,0}s_{fc}, \\ f_r &= f_{r,0}s_{fr}, \\ v_g &= v_{g,0}s_{vg}, \\ v_s &= v_{s,0}s_{vs}, \end{aligned} \tag{23}$$

where $f_{c,0}$, $f_{r,0}$, $v_{g,0}$ and $v_{s,0}$ are the rates/speeds, and $s_{f/v}$ are the scaling factors. These scaling factors are determined by optimization which matches model to experiment.

Motor and crosslinker proteins bind to/unbind from MTs. Binding from solution is treated as in previous work [63]. Unbound motors and crosslinkers proteins diffuse through the nucleus according to the equation of motion

$$\mathbf{x}(t + \delta t) = \mathbf{x}(t) + \delta\mathbf{x}(t), \tag{24}$$

where the proteins diffuse in the nuclear volume with diffusion constant D_{free}. Upon reaching the nuclear envelope, motor and crosslinker proteins reflect inward into the nuclear volume.

Once a motor/crosslinker is within a distance of R_{cap} of the MT, it can bind one head according to the on-rate

$$k_{01}(\mathbf{r}_m, \mathbf{r}_{\mathrm{MT}}, \mathbf{u}_{\mathrm{MT}}) = K_a^i \frac{3\epsilon k_0^{s,i}}{4\pi R_{\mathrm{cap}}^3}\alpha l_{in}(\mathbf{r}_m, \mathbf{r}_{\mathrm{MT}}, \mathbf{u}_{\mathrm{MT}}), \tag{25}$$

where K_a^i is the association constant of head i, ϵ is the linear binding site density of an MT, $k_0^{s,i}$ is the turnover rate for protein head i in the singly to unbound transition, R_{cap} defines the radius of the binding sphere for the transition, α is a scaling factor for the weak dependence of the rate on the total filament length [63], and l_{in} is the length of the filament defined by $\mathbf{r}_{\mathrm{MT}}$ and $\mathbf{u}_{\mathrm{MT}}$ lying within R_{cap} of the crosslinker at position $\mathbf{r}_m$. In our simulations K_a^i and ϵ are multiplied together. Singly bound motor/crosslinker heads detach at a constant rate

$$k_{10} = k_0^{s,i}\alpha, \tag{26}$$

where the α is the same scaling factor used above.

The binding of the second motor/crosslinker head to nearby MTs is force-dependent and depends on the stretch/compression of the tether spring. Detachment from the doubly bound state occurs at rate

$$k_{21}(\mathbf{r}_a, \mathbf{r}_b) = k_{1,\alpha}\exp\left[\beta x_c K_m(|\mathbf{r}_b - \mathbf{r}_a| - R_{m,0})\right], \tag{27}$$

bioRxiv preprint doi: https://doi.org/10.1101/649913; this version posted October 22, 2019. The copyright holder for this preprint (which was not certified by peer review) is the author/funder. All rights reserved. No reuse allowed without permission.

Kinetochore kinematics	**Symbol**	**Value**	**Notes**
Diameter	σ_{KC}	200 nm	[63, 77]
Length	$L_{KC,0}$	150 nm	[98]
Width	$L_{KC,1}$	50 nm	[98]
Thickness	d_{KC}	0 nm	Chosen
Diffusion coefficient	D_{KC}	5.9×10^{-4} μm^2 s^{-1}	[52, 63, 77]
Translational drag	$\gamma_{KC,t}$	3.51 pN μm^{-1} s	Computed
Rotational drag	$\gamma_{KC,r}$	0.165 pN μm s	Computed
Catastrophe enhancement	$s_{\mathrm{KC-cen,fc}}$	0.0828 pN^{-1}	Matches NE factor
MT tip length	$l_{\mathrm{cen,tip}}$	25 nm	Chosen
Interkinetochore spring			
Rest length	$R_{C,0}$	100 nm	[52, 105, 129]
Linear spring constant	κ_C	39 pN μm^{-1}	Optimized
Rotational spring constant	$\kappa_{C,u}$	1850 pN nm rad^{-1}	Optimized
Alignment spring constant	$\kappa_{C,v}$	1850 pN nm rad^{-1}	Optimized
Pericentric chromatin			
Pericentric chromatin length	$r_{\mathrm{centromere}}$	200 nm	Chosen
Pericentric chromatin diameter	$d_{\mathrm{centromere}}$	75 nm	Chosen
Kinetochore-centromere offset	$r_{\mathrm{KC-cen}}$	37.5 nm	Chosen
Chromatin-MT repulsion amplitude	A_{CMT}	1 pN nm	Optimized

Table 4: Chromosome and kinetochore parameters.

where k_{21} is the off-rate, $k_{1,\alpha}$ is the base rate, $\mathbf{r}_a$ and $\mathbf{r}_b$ are the locations of the motor or crosslinker heads, β is the inverse temperature, x_c is the characteristic distance describing force-dependent off-rates, K_m is the motor/crosslinker spring constant, and $R_{m,0}$ is the rest length of the spring. The corresponding on-rate is

$$k_{12}(\mathbf{r}_a, \mathbf{r}_{MT}, \mathbf{u}_{MT}) = k_{1,\alpha} c_2 \int \exp\left[-\frac{\beta K_m}{2}(|\mathbf{r}(s)| - R_{m,0})^2 + \beta x_c K_m (|\mathbf{r}(s)| - R_{m,0})\right] ds, \quad (28)$$

where c_2 is the effective binding concentration, and $\mathbf{r}(s)$ is the distance between the already bound motor head position $\mathbf{r}_a$ and the position on the second MT denoted by the linear variable s

$$\mathbf{r}(s) = \mathbf{r}_{MT} + s\hat{\mathbf{u}}_{MT} - \mathbf{r}_a, \quad (29)$$

where $\mathbf{r}_{MT}$ is the center of mass of the MT filament, $\hat{\mathbf{u}}_{MT}$ is the orientation of the MT, and s is the linear distance of the second crosslinker head.

A.1.6 Chromosomes

Chromosomes contain the genetic material of the cell whose segregation is the primary purpose of mitosis. Sister chromatids are held together by cohesin [105, 129, 165]. Each duplicated sister chromatid assembles the kinetochore onto the centromeric DNA region during mitosis. The outer kinetochore forms the primary MT attachment site for the chromosomes through the KMN (or in yeast, MIND) networks/complexes [21, 108, 166–170]. This network/complex contains the Ndc80, KNL1, Mis12, and

bioRxiv preprint doi: https://doi.org/10.1101/649913; this version posted October 22, 2019. The copyright holder for this preprint (which was not certified by peer review) is the author/funder. All rights reserved. No reuse allowed without permission.

Dam/DASH proteins/complexes, and is also important for kinetochore signaling and lost kinetochore recapture [77,110,171]. Chromosomes and kinetochores also contain Aurora B kinase (Ark1 in *S. pombe*), an essential spindle checkpoint component. Aurora B destabilizes incorrect attachments found between the kinetochore and MTs when the chromosome is mis-aligned [40–42,172–174].

Chromosomes are modeled as sister pairs of chromatids, centromeric DNA, and kinetochores, attached to each other prior to anaphase via a spring potential. We assume that chromosomes do not interact with particles in the spindle, except through the binding/unbinding of attachments at kinetochores, steric repulsion with the nuclear envelope and MTs. A kinetochore moves as a sphere in a viscous medium

$$\mathbf{x}(t+\delta t) = \mathbf{x}(t) + \frac{1}{\gamma_{KC,t}}\mathbf{F}(t)\delta t + \delta\mathbf{x}(t), \tag{30}$$

where $\mathbf{F}(t)$ is the applied force, γ_t is the translational drag of the kinetochore, and $\delta\mathbf{x}(t)$ is normally distributed random noise with variance $\langle\delta\mathbf{x}(t)\delta\mathbf{x}(t)\rangle = 2D_{KC}\mathbf{I}\delta t$. D_{KC} is the diffusion coefficient of a lost kinetochore [77]. Kinetochores have principal axes that define their orientation with unit vectors $\hat{\mathbf{u}}$ the outward facing normal of the kinetochore, $\hat{\mathbf{v}}$ along the long arm of the centromeric DNA, and $\hat{\mathbf{w}}$ perpendicular to these (along the short edge of the kinetochore). The equations of motions are

$$\hat{\mathbf{u}}_i(t+\delta t) = \hat{\mathbf{u}}_i(t) + \frac{1}{\gamma_{KC,r}}\mathbf{T}(t)\times\hat{\mathbf{u}}_i(t)\delta t + \delta\hat{\mathbf{u}}_i(t), \tag{31}$$

where i denotes the unit vector in ($\hat{\mathbf{u}}$, $\hat{\mathbf{v}}$, $\hat{\mathbf{w}}$), $\mathbf{T}(t)$ is the torque on the kinetochore, and two random Gaussian noise terms are added to $\hat{\mathbf{v}}$ and $\hat{\mathbf{w}}$ with variance

$$\langle\delta\hat{\mathbf{u}}_i(t)\delta\hat{\mathbf{u}}_i(t)\rangle = \frac{2k_BT}{\gamma_{KC,r}}(\hat{\mathbf{I}} - \hat{\mathbf{u}}\hat{\mathbf{u}})\delta t. \tag{32}$$

Kinetochores experience steric repulsion via the WCA potential with the nuclear envelope with a potential

$$u_{\mathrm{wca,KC}}(r_{\min}) = \begin{cases} 4k_BT\left[\left(\frac{\sigma}{r_{\min}}\right)^{12} - \left(\frac{\sigma}{r_{\min}}\right)^{6}\right] + k_BT, & r_{\min} < 2^{1/6}\sigma, \\ 0, & r_{\min} \geq 2^{1/6}\sigma, \end{cases} \tag{33}$$

where $r_{\min}$ is the minimum distance between the center of the kinetochore and the enclosing sphere of radius $R + (\sigma_{\mathrm{KC}}/2)$. The chromatin does not interact with the nuclear envelope in the model.

Kinetochore plaques are two-dimensional, with long axis $L_{KC,0}$ along the centromeric DNA region and short axis $L_{KC,1}$ perpendicular to this region. Because MTs were not observed to pass through kinetochores in fission yeast spindle tomographic reconstructions [98], we included a steric repulsion between the plaques and MTs of the form

$$u_{\mathrm{wca,MT-KCmesh}}(r_{\min}) = \begin{cases} 4k_BT\left[\left(\frac{\sigma}{r_{\min}}\right)^{12} - \left(\frac{\sigma}{r_{\min}}\right)^{6}\right] + k_BT, & r_{\min} < 2^{1/6}\sigma, \\ 0, & r_{\min} \geq 2^{1/6}\sigma, \end{cases} \tag{34}$$

where $r_{\min}$ is the minimum distance from the MT to the triangulated kinetochore mesh, and σ defines half of the MT diameter to approximate an infinitely thin kinetochore. This force contributes to force-induced catastrophe when the MT tip interacts with the kinetochore.

bioRxiv preprint doi: https://doi.org/10.1101/649913; this version posted October 22, 2019. The copyright holder for this preprint (which was not certified by peer review) is the author/funder. All rights reserved. No reuse allowed without permission.

The centromeric DNA regions is modeled as a spherocylinder with length $r_{\text{centromere}}$ and diameter $d_{centromere}$. Kinetochore plaques are located on the surface of these regions, with an offset from the center of the centromeric DNA chromatid of $r_{\text{KC-cen}}$. Centromeric DNA regions experience a weak repulsive interaction with MTs of the form

$$u_{\text{gauss}}(r_{\text{min}}) = \frac{A_{CMT}}{\sigma\sqrt{2\pi}} \exp\left[\frac{-r_{\text{min}}^2}{2\sigma^2}\right], \tag{35}$$

where $\sigma = d_{\text{centromere}}/10 + \sigma_{\text{MT}}/10$, A_{CMT} sets the maximum repulsion, and r_{min} is the minimum distance between the chromatin spherocylinder and the MT spherocylinder. The strength of this potential is set on the order of 1 k_BT, and contributes to MT force-induced catastrophe.

Sister chromosomes, chromatids, and kinetochores are bound to each other until anaphase by linear and angular springs. Each centromeric DNA region has a right-handed coordinate system that is determined at the beginning of the simulation, and defines the principle axes of the chromatid/centromeric DNA region/kinetochore ($\hat{\mathbf{u}}_i$, $\hat{\mathbf{v}}_i$, $\hat{\mathbf{w}}_i$), where i now labels the sister of the pair. For the interkinetochore spring, $\hat{\mathbf{u}}_i$ is the outward-facing normal of the first kinetochore, and the inward-facing normal of the second kinetochore, and $\hat{\mathbf{v}}_i$ points along the chromatid arm. The potential is

$$u_{\text{chromosome}} = \frac{1}{2}\kappa_C(r - R_{C,0})^2 + \frac{1}{2}\kappa_{C,u}(\theta_A^2 + \theta_B^2) + \frac{1}{2}\kappa_{C,v}\theta_v^2, \tag{36}$$

where $\mathbf{r} = \mathbf{r_A} - \mathbf{r_B}$, $r = |\mathbf{r}|$, $cos(\theta_{A,B}) = \hat{\mathbf{u}}_{A,B} \cdot \hat{\mathbf{r}}$ and $cos(\theta_v) = \hat{\mathbf{v}}_A \cdot \hat{\mathbf{v}}_B$. This potential serves to align the sister kinetochores/chromatids so that they are back-to-back with inter-kinetochore distance $R_{C,0}$ and aligning spring constants κ_C, $\kappa_{C,u}$, and $\kappa_{C,v}$.

The forces and torques on the chromatids due to the interkinetochore potential (Equation 36) is computed as in previous work [175]. The force on chromatid A is

$$\mathbf{f}_A = -\kappa_C(r - R_{C,0})\hat{\mathbf{r}} - \frac{\kappa_{C,u}}{r}\left[\frac{\theta_A}{\sin(\theta_A)}(\hat{\mathbf{r}} \times (\hat{\mathbf{r}} \times \hat{\mathbf{u}}_A)) + \frac{\theta_B}{\sin(\theta_B)}(\hat{\mathbf{r}} \times (\hat{\mathbf{r}} \times \hat{\mathbf{u}}_B))\right]. \tag{37}$$

The force on chromatid B is equal and opposite. The torques are

$$\tau_A = -\kappa_{C,u}\left[\frac{\theta_A}{\sin(\theta_A)}(\hat{\mathbf{r}} \times \hat{\mathbf{u}}_A)\right] + \kappa_{C,v}\left[\frac{\theta_v}{\sin(\theta_v)}(\hat{\mathbf{v}}_A \times \hat{\mathbf{v}}_B)\right], \tag{38}$$

$$\tau_B = -\kappa_{C,u}\left[\frac{\theta_B}{\sin(\theta_B)}(\hat{\mathbf{r}} \times \hat{\mathbf{u}}_B)\right] - \kappa_{C,v}\left[\frac{\theta_v}{\sin(\theta_v)}(\hat{\mathbf{v}}_A \times \hat{\mathbf{v}}_B)\right]. \tag{39}$$

These can be checked for validity by using $\mathbf{r} \times \mathbf{f_A} + \tau_\mathbf{A} + \tau_\mathbf{B} = \mathbf{0}$.

There are 3 (N_{AF}) kinetochore-MT binding sites on average in fission yeast with inter-binding site spacing $r_{AF,ex}$ of 40 nm [98]. Kinetochore-MT attachments are modeled as a linear and angular spring

$$u_{AF} = \frac{1}{2}\kappa_m(r(s) - r_0)^2 + \frac{1}{2}\kappa_r(\hat{\mathbf{u}}_{KC} \cdot \hat{\mathbf{r}}(s) - 1)^2, \tag{40}$$

where κ_m is the linear spring constant, r_0 is the rest length of the attachment, κ_r is the angular spring constant, and $\hat{\mathbf{u}}_{\text{KC}}$ is now the outward-facing normal orientation of the kinetochore. The vector $\mathbf{r}(s)$ is

bioRxiv preprint doi: https://doi.org/10.1101/649913; this version posted October 22, 2019. The copyright holder for this preprint (which was not certified by peer review) is the author/funder. All rights reserved. No reuse allowed without permission.

the distance from the kinetochore binding site location on the kinetochore to the attachment site on the MT

$$\mathbf{r}(s) = \mathbf{r}_{MT} + s\hat{\mathbf{u}}_{MT} - \mathbf{r}_{AF}, \tag{41}$$

where $\mathbf{r}_{AF}$ is the coordinate of the kinetochore binding site. Forces and torques from this potential are also calculated according to [175], with the force on the bound MT from the kinetochore

$$\mathbf{f}_{MT} = -\kappa_m(r - r_0)\hat{\mathbf{r}} + \frac{\kappa_r}{r}(\hat{\mathbf{u}}_{KC} \cdot \hat{\mathbf{r}} - 1)\left[\hat{\mathbf{r}} \times (\hat{\mathbf{r}} \times \hat{\mathbf{u}}_{KC})\right], \tag{42}$$

where $r = |\mathbf{r}(s)|$. The torque on the kinetochore is

$$\tau_{KC} = \kappa_r(\hat{\mathbf{u}}_{KC} \cdot \hat{\mathbf{r}} - 1)(\hat{\mathbf{r}} \times \hat{\mathbf{u}}_{KC}). \tag{43}$$

Kinetochore-MT attachments have been shown to have force-dependent lifetime [100, 101]. The on-rate for kinetochores binding MTs is analogous to that of motor and crosslinker proteins with an additional the angular term

$$k_{on} = k_0 c_{on} \int \exp\left[-\frac{\beta\kappa_m}{2}(r(s) - r_0)^2 + x_c\beta\kappa_m(r(s) - r_0) - \frac{\beta\kappa_r}{2}(\hat{\mathbf{u}}_{KC} \cdot \hat{\mathbf{r}} - 1)^2 - \chi_c\beta\kappa_r(\hat{\mathbf{u}}_{KC} \cdot \hat{\mathbf{r}} - 1)\right] ds, \tag{44}$$

where x_c is the linear characteristic distance of the force-dependent interaction, and χ_c controls the angular force dependence. Notice that for the χ_c enhancement to the angular rate, we are choosing the more numerically stable factor of $f_\theta = -\chi_c K_r(\hat{\mathbf{u}}_{KC} \cdot \hat{\mathbf{r}} - 1)$. The accompanying off-rate is

$$k_{\text{off}} = k_0 \exp\left[x_c\beta\kappa_m(r - r_0)\right] \exp\left[-\chi_c\beta\kappa_r(\hat{\mathbf{r}} \cdot \hat{\mathbf{u}}_{KC} - 1)\right], \tag{45}$$

where $r = |\mathbf{r}|$ is the distance between the binding site location on the kinetochore and the MT binding location, and $\hat{\mathbf{r}}$ is the orientation of this separation. These rates are only calculated every N_{kmc} steps because of the complexity involved in their evaluation.

Kinetochores affect MT dynamic instability in a force-dependent manner when attached to MT plus-ends. This affects the growing speed, shrinking speed, rescue frequency and catastrophe frequency in the form

$$k(F) = k_0 \exp\left[\frac{F}{F_c}\right], \tag{46}$$

where F_c is the characteristic force, and $k(F)$ and k_0 are the force-dependent and base speed/frequency.

Kinetochores can bind both MT lateral walls and plus-ends with different binding affinity ($c_{AF,tip}$ the effective concentration for the plus-end, $c_{AF,side}$ the effective concentration for MT lateral wall, $k_{AF,tip,a}$ the rate for attaching to an assembling MT tip, $k_{AF,tip,d}$ the rate for attaching to a disassembling MT tip, and $k_{AF,side}$ the rate for attaching to the MT wall, Table 5) [77, 100, 177]. The tip region of the MT is defined by $l_{AF,tip}$, and only kinetochores bound in this region can affect MT dynamic instability. Attachments bound to the tip have MT-polymerization-state-dependent lifetime. We require that only one attachment factor can bind to the same MT tip ($b_{AF,tip}$), and so if two or more are found bound to the same tip, the attachment factor farther from the tip is unbound.

Progressive restriction of kinetochore-MT attachment is modeled by changing the angular spring constant based on the number of bound MTs

$$\kappa_r = \kappa_r(N_a), \tag{47}$$

bioRxiv preprint doi: https://doi.org/10.1101/649913; this version posted October 22, 2019. The copyright holder for this preprint (which was not certified by peer review) is the author/funder. All rights reserved. No reuse allowed without permission.

Parameter	**Symbol**	**Value**	**Notes**
Number	N_{AF}	3	[98]
Attachment site separation on kinetochore	$r_{AF,ex}$	40 nm	[98]
Linear spring constant	$\kappa_{AF,m}$	0.088 pN nm^{-1}	Optimized
Angular spring constant, 0 to 1	$\kappa_{AF,r,0}$	4.1 pN nm	Optimized
Angular spring constant, 1 to 2	$\kappa_{AF,r,1}$	41 pN nm	Optimized
Angular spring constant, 2 to 3	$\kappa_{AF,r,2}$	410 pN nm	Optimized
Angular spring constant, 3 to 3	$\kappa_{AF,r,3}$	410 pN nm	Optimized
Rest length	$r_{AF,0}$	54 nm	[176]
kMC steps	N_{kmc}	10	Chosen
MT tip length	$l_{AF,tip}$	25 nm	Chosen
MT tip crowding	$b_{AF,tip}$	True	[98]
Tip concentration	$c_{AF,tip}$	40 nm^{-1}	Optimized
Side concentration	$c_{AF,side}$	0.4 nm^{-1}	Optimized
Tip rate assembling	$k_{AF,tip,a}$	0.0001 s^{-1}	Optimized
Tip rate disassembling	$k_{AF,tip,d}$	0.03 s^{-1}	Optimized
Side rate	$k_{AF,side}$	0.03 s^{-1}	Optimized
Tip characteristic distance assembling	$x_{c,t,a}$	1 nm	Optimized
Tip characteristic distance disassembling	$x_{c,t,d}$	-3.9 nm	Optimized
Side characteristic distance	$x_{c,s}$	-0.37 nm	Optimized
Angular characteristic factor	χ_c	0.013	Optimized
Speed	v_{AF}	50 nm s^{-1}	Optimized
Stall force	$f_{AF,stall}$	5 pN	Kinesin-5 [63, 99]
Tip diffusion	D_{tip}	0.0012 μm^2 s^{-1}	Optimized
Side diffusion	D_{side}	0.018 μm^2 s^{-1}	Optimized
Tip tracking	$f_{AF,track}$	0.25	Optimized
Tip-enhanced catastrophe	$s_{fc,dam1}$	4	Optimized
Misaligned destabilization	$s_{k,ABK}$	70	Optimized
Polymerization force factor	$F_{AF,vg}$	8.4 pN	[52, 100]
Depolymerization force factor	$F_{AF,vs}$	-3.0 pN	[52, 100]
Catastrophe force factor	$F_{AF,fc}$	-2.3 pN	[52, 100]
Rescue force factor	$F_{AF,fr}$	6.4 pN	[52, 100]
Maximum polymerization speed	$v_{AF,MT,max}$	30 μm min^{-1}	[52]

Table 5: Attachment factor parameters.

where κ_r is the angular spring constant and N_a the number of bound MTs to the kinetochore. Note that each kinetochore can have a different number of attachments, and there is an angular spring constant for unbound kinetochores that controls the binding rate of lost kinetochores.

Kinetochore attachments are mobile on MTs, and they diffuse along MTs, track MT ends when attached at the tip, and can have directed motion [99, 178]. These attachments move on MTs according to

$$x_l(t+\delta t) = x_l(t) + v(\mathbf{F}, \mathbf{u}_{\mathrm{MT}})\delta t + \beta D_l \mathbf{F} \cdot \mathbf{u}_{\mathrm{MT}} \delta t + f_{AF,track} d_{poly} + \delta x_l(\delta t), \tag{48}$$

bioRxiv preprint doi: https://doi.org/10.1101/649913; this version posted October 22, 2019. The copyright holder for this preprint (which was not certified by peer review) is the author/funder. All rights reserved. No reuse allowed without permission.

where $l_{AF,tip}$ denotes if the attachment is in the MT tip region, $\mathbf{F}$ is the force on the attachment, $\mathbf{u}$ is the orientation of the MT, D_l is the one-dimensional diffusion coefficient of the attachment on the MT (D_{tip} for MT tips, D_{side} for sides), $f_{AF,track}$ is the tip-tracking fraction, and d_{poly} is the distance the MT polymerized in the last time step (this effect is only turned on for MT tips). The random displacement term $\delta x_l(t)$ is Gaussian random noise with variance $2D_l\delta t$. Attachments between kinetochores and MTs do not detach when they reach MT tips. The kinetochore motor force-velocity relation is linear, as for crosslinking motors,

$$v(\mathbf{F}, \mathbf{u}_{\mathrm{MT}}) = v_0 \max\left(0, \min\left(1, 1 + \mathbf{u}_{\mathrm{MT}} \cdot \frac{\mathbf{F}}{f_{stall}}\right)\right), \tag{49}$$

where f_{stall} is the stall force of the attachment and v_0 is the speed.

When an attachment factor is bound near an MT tip, the MT dynamics are destabilized by a combination of proteins, and this is represented in the model by the enhanced catastrophe factor $s_{fc,dam1}$. This has the effect of multiplying the base catastrophe rate by this constant.

A.1.7 Kinetochore-MT attachment error correction models: biorientation-dependent and force-dependent

In the initial formulation of the model, we implemented a rule that kinetochore-MT attachments in the model are destabilized when the chromosome is not bioriented. In this case, each attachment and detachment rate is multiplied by the factor $s_{k,ABK}$ to maintain the binding equilibrium between the on- and off-rates

$$k_{AF} = \begin{cases} k_{AF}, & \text{amphitelic}, \\ s_{ABK} k_{AF}, & \text{misaligned}, \end{cases} \tag{50}$$

where k_{AF} is the rate of the kinetochore-MT attachment or detachment and s_{ABK} is the misaligned destabilization factor.

To make the error-correction model more mechanistic, we also tested a version of force-dependent error correction, building on previous results that show that kinetochore-MT attachments are stabilized by force [120,121]. We made the kinetics of kinetochore-MT attachments dependent on interkinetochore tension in the form

$$k_{AF} = \frac{k_{\mathrm{AF},0}}{1 + \frac{F}{F_{\mathrm{EC},0}}} \text{ when } \mathbf{F} \cdot \mathbf{u}_{KC} < 0, \tag{51}$$

where F is the interkinetochore force and and $F_{\mathrm{EC},0}$ is a characteristic force for significant stabilization: when the interkinetochore tension reaches the value $F_{\mathrm{EC},0}$, the rate drops by a factor of two from its unstabilized value. Therefore, smaller values of $F_{\mathrm{EC},0}$ correspond to higher force sensitivity. This stabilization is only active when the force on the kinetochore is in the opposite direction of the kinetochore outward facing normal orientation. Only kinetochore-MT attachment off-rates are reduced when there is interkinetochore tension.

We carried out several rounds of optimization for the force-dependent error correction model, as initial models did not lead to biorientation. Recent work has shown that kinetochores may experience tension before biorientation [38], and so we varied additional parameters in the model to facilitate tension generation prior to biorientation. These parameters were the angular spring constants of the interkinetochore spring ($\kappa_{C,u}$ and $\kappa_{C,v}$), the characteristic angular factor for binding high angles to the kinetochore

bioRxiv preprint doi: https://doi.org/10.1101/649913; this version posted October 22, 2019. The copyright holder for this preprint (which was not certified by peer review) is the author/funder. All rights reserved. No reuse allowed without permission.

Parameter	Symbol	Value	Notes
Inter-kinetochore stabilization force	$F_{\mathrm{EC},0}$	1.67 pN	Optimized
Rotational spring constant	$\kappa_{C,u}$	925 pN nm rad^{-1}	Optimized
Alignment spring constant	$\kappa_{C,v}$	925 pN nm rad^{-1}	Optimized
Angular characteristic factor	χ_c	0.08	Optimized
Side concentration	$c_{AF,side}$	0.32 nm^{-1}	Optimized
Kinesin-5 number	N_{K5}	200	Optimized

Table 6: Force-dependent error correction model parameters.

Anaphase	Symbol	Value	Notes
Integrated simultaneous biorientation time	τ_{SAC}	4.45 min	Chosen
Anaphase attachment rate	$k_{AF,anaphase}$	0.00007 s^{-1}	Chosen
Anaphase MT depoly speed	$v_{anaphase,s,0}$	2.2 μm min^{-1}	Chosen

Table 7: Anaphase parameters

plate χ_C, the effective concentration for binding to lateral walls of MTs $c_{AF,side}$, and the number of kinesin-5 motors N_{K5}, which affect overall spindle force generation. We identified model parameters that favored end-on over lateral attachments, inhibited attachments at high angle, and allowed sister kinetochores to more easily reorient (Table 6).

A.1.8 Anaphase

Anaphase is triggered by waiting until all three chromosomes are bioriented simultaneously for a time τ_{SAC}. Then the potential connecting the two sister chromatids is removed, and misaligned destabilization is turned off ($s_{k,ABK} = 1$). The rates governing kinetochore-MT attachment are modified to all be the same value ($k_{AF,anaphase}$), and kinetochore MTs are forced to undergo depolymerization. Finally, the MT shrinking speed is changed to be $v_{anaphase,s,0}$.

A.1.9 Initial conditions

At the beginning of mitosis in *S. pombe* the two SPBs are linked by a bridge [179, 180]. Initially the spindle pole bodies are placed adjacent with their center separated by the spindle pole body diameter plus the bridge size $\sigma_{\mathrm{SPB}} + 75$ nm. MTs are inserted randomly onto each SPB so that they do not overlap and are within the nuclear volume. Initially MTs are their minimum length (75 nm) and in the paused dynamic instability state. Motors and crosslinkers are randomly inserted into the nucleus. Chromosomes are placed near the spindle pole bodies, with a single attachment between one kinetochore and the first spindle pole body. Simulations are started with SPBs fixed for a linkage time τ_{link}.

A.2 Parameter constraint and model refinement

The constrain unmeasured parameters, we performed refinement and optimization, based on previous work [63]. To do this, we measured spindle length and movement of a single sister kinetochore pair for 9 cells (as discussed in experimental methods below). The fitness function defined to compare simulation and experiment includes three contributions. (1) Spindle structure fitness is based on spindles

bioRxiv preprint doi: https://doi.org/10.1101/649913; this version posted October 22, 2019. The copyright holder for this preprint (which was not certified by peer review) is the author/funder. All rights reserved. No reuse allowed without permission.

reconstructed from electron tomography. (2) The dynamics of spindle length, kinetochore movement, and interkinetochore separation were compared to fluorescence microscopy (3) We sought to maximize the amount of time all chromosomes are bioriented.

The spindle structural parameters were similar to those used in previous work [63]. The length distribution of MTs, the length distribution of interpolar MTs, the maximum pairing length, and the angular distribution of MTs relative to the spindle axis from three different tomographic reconstructions of fission-yeast spindles of different lengths are compared to simulation results. Spindles matching the target length ± 50 nm are used to determine distributions from simulation. All measurements from all runs at a particular parameter point are compiled into one distribution for comparison with tomographic data. The EM fitness is defined as

$$f_{\mathrm{EM,i,l}} = \begin{cases} -10, & p = 0, \\ \frac{log_{10}(p_{i,l})}{100}, & p > 0, \end{cases} \tag{52}$$

where i labels the distribution and l the target length. The p-value from the Kolmogorov-Smirnov (KS) test of the combined measurements in the model is used as the input to this function. The total EM fitness is the average

$$f_{\mathrm{EM}} = \frac{1}{3} \sum_{\mathrm{length}} \frac{1}{4} \sum_{\mathrm{distribution}} f_{EM,i,l}. \tag{53}$$

The value of this objective function lies in (-10, 0), where a larger value indicates a better match.

We measured spindle length, kinetochore position, and interkinetochore distance. To quantify similarity between simulated and experimental measurements, we computed the Pearson correlation coefficient with simulation data sampled at same time as experimental measurements. Spindle length fitness is

$$f_{\mathrm{L}}(s,t) = \rho_{\mathrm{L}}(s,t), \tag{54}$$

where s labels the simulation, t labels a distinct experimental trace of spindle length versus time, and ρ is the Pearson correlation coefficient. When comparing the dynamics of kinetochore distance from a single spindle pole, we find the maximum Pearson correlation coefficient to determine which spindle pole to use in the analysis. The spindle pole body-kinetochore fitness is

$$f_{\mathrm{SPB-KC}}(s,t) = \frac{1}{2N_c} \sum_c \max(\rho_{1,1,\mathrm{c}} + \rho_{2,2,\mathrm{c}}, \rho_{1,2,\mathrm{c}} + \rho_{2,1,\mathrm{c}}), \tag{55}$$

where N_c is the number of chromosomes, c sums over the chromosomes, and $\rho_{1,1,c}$ is the Pearson correlation coefficient for comparing kinetochore 1 in the simulation to kinetochore 1 in the experiment, and so on. The interkinetochore separation has fitness

$$f_{\mathrm{KC-KC}}(s,t) = \frac{1}{N_c} \sum_c \rho_{\mathrm{KC-KC,c}}, \tag{56}$$

where $\rho_{\mathrm{KC-KC,c}}$ is the Pearson correlation coefficient of interkinetochore separation of chromosome c. The dynamic fitness function is then

$$f_{\mathrm{d}}(s,t) = f_{\mathrm{L}} + f_{\mathrm{SPB-KC}} + f_{\mathrm{KC-KC}}. \tag{57}$$

bioRxiv preprint doi: https://doi.org/10.1101/649913; this version posted October 22, 2019. The copyright holder for this preprint (which was not certified by peer review) is the author/funder. All rights reserved. No reuse allowed without permission.

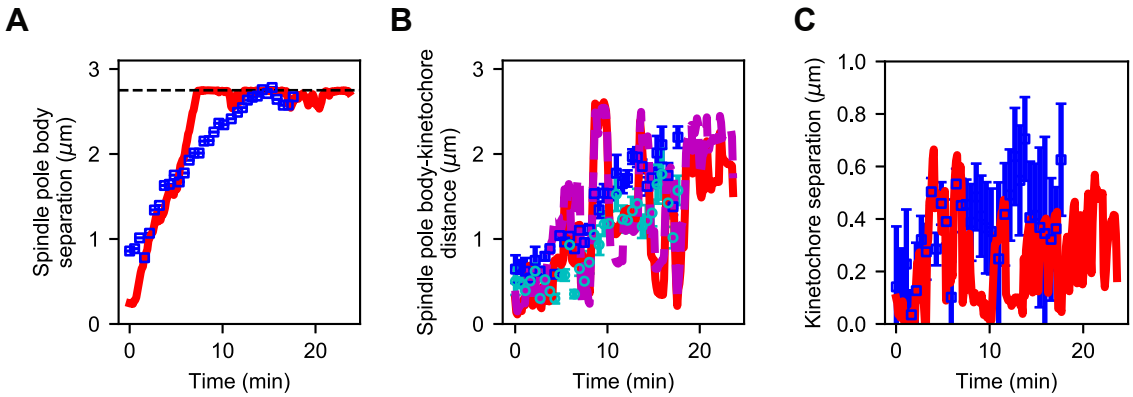

Figure 10: **Reference model generates similar dynamics of spindle length and kinetochore position compared to experiment.** (**A**) Spindle length versus time for experiment (blue) and refined model (red). (**B**) Spindle pole body-kinetochore distance versus time for a single kinetochore pair (Cen2) in experiment (blue, cyan) and refined model (red, magenta). (**C**) Kinetochore separation versus time for experiment (blue) and refined model (red). This comparison gives Pearson correlation coefficients for length = 0.891, SPB-KC distance = 0.72, Interkinetochore distance = 0.42.

For each set of simulation parameters, the dynamic fitness is averaged over all simulated and experimental time traces.

To promote long-lived simultaneous biorientation of all chromosomes and end-on kinetochore attachments to MTs, we measure the fraction of simultaneous biorientation

$$f_{\mathrm{I}} = \frac{\sum_i f_a^1(i) f_a^2(i) f_a^3(i)\,[L(i) > 1\mu m]}{\sum_i 1}, \tag{58}$$

where i is the time, $f_a^c(i)$ is 1 if chromosome c has amphitelic attachment at time i, and $L(i)$ is the spindle length at time i. This value is larger when all three chromosomes are simultaneously bioriented for longer time. Next we measure the weighted average number of attachments

$$f_{\mathrm{b}} = \frac{\sum_{i,c} f_a^c(i) N_a^c(i)}{\sum_{i,c} N_{\max}}, \tag{59}$$

where N_a^c is the number of end-on attachments of chromosome c at time i and $N_{\max}$ is the maximum number of kinetochore attachments per chromosome at time i (6 per chromosome).

The total fitness is the weighted sum

$$f = f_d + f_{\mathrm{EM}} + 2f_{\mathrm{I}} + 2f_{\mathrm{b}}. \tag{60}$$

Note the possible values of each fitness: f_{d} can take values (-3, 3), f_{EM} (-10, 0), and f_{I} and f_{b} (0, 1), which are weighted in the total fitness to (0, 2). The total fitness therefore falls in the range (-13, 7). The reference model has a total fitness of 3.36 with dynamic fitness 1.23, EM fitness -0.10, fraction simultaneous biorientation 0.68, and weighted average number of attachments 0.43. An example of model/experiment comparison is shown in Figure 10.

bioRxiv preprint doi: https://doi.org/10.1101/649913; this version posted October 22, 2019. The copyright holder for this preprint (which was not certified by peer review) is the author/funder. All rights reserved. No reuse allowed without permission.

A.2.1 Optimization of parameters

We optimized unknown or poorly constrained parameters, as in previous work [63]. We attempted to use particle-swarm optimization [181] by first randomly sampling parameter sets, and then refining the parameters to reach maximum fitness. However, for our high-dimensional optimization we found slow convergence, and used human input to guide the particle swarm. This included scans of single parameters identify parameter ranges that increased the total fitness.

Unknown or poorly constrained parameters that we optimized include the stabilization parameters of MTs in bundles and the number and force-sensitivity of the motors and crosslinkers (Tables 1, 3). We note that the characteristic distances found for force-dependent unbinding are similar to previously measured kinesin force-dependence [160]. For the chromosome and kinetochore model, we optimized multiple parameters. The linear and angular spring constants of interkinetochore interactions were initially taken from previous models, then optimized to their own values (Table 4) [105, 129]. We also optimized the strength of the soft repulsion between chromatin and MTs; the angular spring constants for progressive locking; concentration, rate, and characteristic distance kinetochore-MT attachments [100]; the movement of kinetochore-MT attachments on MTs; the amount of enhanced catastrophe from attachments at MT plus-ends; and the amount misaligned attachments are destabilized (Table 5).

A.3 Experimental methods

The fission-yeast strain includes *cen2-GFP* to label centromeric DNA with lacI-GFP of chromosome 2 (Table 8) [104]. The microtubules were tagged with low-level labeling of *mCherry-atb2* [103]. 9 cells which began in interphase were continuously imaged through anaphase B. The time-lapse images shown in Figure 2E and Figure 8E were taken using live cell preparation and spinning-disk confocal imaging on a Nikon Eclipse Ti microscope as previously described [52, 63]. Cell temperature was maintained at 25C with a CherryTemp temperature control device (Cherry Biotech, Rennes, France) with an accuracy of +/-0.1C. 3D images were obtained with an EM Gain of 300 and an exposure time of 100 ms for the 488 nm laser and 150 ms for the 561 nm laser, both at 100% laser power. 7 planes were acquired in the z dimension with 500 nm separation between each plane. Images are displayed as smoothed maximum-intensity projections with $\sim$8 seconds between successive images and were prepared using Image J software (NIH, Bethesda, Maryland).

Analysis of experimental images was performed in MATLAB by extending previous work [106]. Individual cells were segmented using morphology and geometric considerations on time-averaged and space-convolved videos to find locations of objects persisting in both space and time. Using the microtubule channel, only cells that at some point exhibited a bright spindle were segmented. After segmentation, the position of each object was estimated. The first SPB location was estimated to be at the location of the brightest pixel in the image in the MT channel. We estimated spindle orientation by thresholding the image to find the brightest $\sim$10 pixels, and then estimated the spindle axis by the direction of the

Name	Genotype	Notes
MB 998	cen2::kanr-ura4$^+$-lacOp, his7$^+$::lacI-GFP, z:adh15:mCherry-atb2:natMX6, leu1-32, h$^-$	This study

Table 8: Strain used in this study.

bioRxiv preprint doi: https://doi.org/10.1101/649913; this version posted October 22, 2019. The copyright holder for this preprint (which was not certified by peer review) is the author/funder. All rights reserved. No reuse allowed without permission.

major axis of the ellipse that encloses the active pixels. The second SPB is assumed to have 80% of the intensity of the first SPB and to lie along the spindle axis. We then estimated a 3D Gaussian line connecting the two SPBs to represent the central MT bundle. Kinetochore positions were estimated by finding peaks in the intensity image in the kinetochore channel. Peaks whose width was comparable to the point spread function were treated as possible kinetochores, and each kinetochore is modeled as a 3D Gaussian.

We fit the position of the objects in the system using a non-linear least squares optimization to minimize the residual error between the raw image and a simulated image using lsqnonlin in MATLAB. This fit varied 13 parameters in the microtubule channel and 13 in the kinetochore channel. Features from multiple time points were tracked. Spindle length was directly determined in each frame, and the two kinetochores were tracked with u-track [106].

A.4 Simulation snapshots and simulated fluorescence images

We generated simulation snapshots amd simulated fluorescence images by first using a quaternion formulation that aligns view orientation vectors with spindle vectors to obtain planar images of the spindle. The algorithm aligns

$$\hat{\mathbf{r}}_{\text{spindle}} \rightarrow \hat{\mathbf{x}}, \tag{61}$$

$$\hat{\mathbf{n}}_{\text{SPBs}} = \frac{\mathbf{r}_{\text{SPB1}} \times \mathbf{r}_{\text{SPB2}}}{|\mathbf{r}_{\text{SPB1}} \times \mathbf{r}_{\text{SPB2}}|} \rightarrow \hat{\mathbf{z}}, \tag{62}$$

where the spindle axis $\hat{\mathbf{r}}_{\text{spindle}}$ is aligned with the unit orientation vector $\hat{\mathbf{x}}$, and the normal of the two SPB vectors $\hat{\mathbf{n}}_{\text{SPBs}}$ is aligned with $\hat{\mathbf{z}}$ (toward the viewer). Simulated fluorescence images are rotated so that the spindle axis lies along the $\hat{\mathbf{y}}$ vector.

Simulated fluorescence images are created by applying a Gaussian blur to every point of the object of interest. For point-like objects such as kinetochores, we applied a 2D Gaussian with the xy point-spread-function and pixel size measured on the microscope. MT fluorescence uses the convolution of a point-Gaussian with the 2-dimensional line

$$\begin{aligned} I(x, y, A, L, \sigma, x_0, y_0, \theta) =& A \exp[(y - y_0)\cos(\theta) + (x_0 - x)\sin(-\theta)] \\ & \{\text{Erf}[\frac{L + (x_0 - x)\cos(\theta) + (y_0 - y)\sin(-\theta)}{\sqrt{2}\sigma}] + \\ & \text{Erf}[\frac{(x_0 - x)\cos(\theta) + (y_0 - y)\sin(-\theta)}{\sqrt{2}\sigma}], \} \end{aligned}$$

where A is the amplitude, L is the length of the line segment, σ is the point-spread, x_0 and y_0 are the starting point of the line segment, and θ is the 2-dimensional direction of the line segment in the xy-plane.